# TOWARD A HALO MASS FUNCTION FOR PRECISION COSMOLOGY: THE LIMITS OF UNIVERSALITY

JEREMY TINKER,[1,2] ANDREY V. KRAVTSOV,[1,2,3] ANATOLY KLYPIN,[4] KEVORK ABAZAJIAN,[5]
MICHAEL WARREN,[6] GUSTAVO YEPES,[7] STEFAN GOTTLÖBER,[8] AND DANIEL E. HOLZ[6]

## ABSTRACT

We measure the mass function of dark matter halos in a large set of collisionless cosmological simulations of flat ΛCDM cosmology and investigate its evolution at $z \lesssim 2$. Halos are identified as isolated density peaks, and their masses are measured within a series of radii enclosing specific overdensities. We argue that these spherical overdensity masses are more directly linked to cluster observables than masses measured using the friends-of-friends algorithm (FOF), and are therefore preferable for accurate forecasts of halo abundances. Our simulation set allows us to calibrate the mass function at $z = 0$ for virial masses in the range $10^{11} \ h^{-1} \ M_\odot \leq M \leq 10^{15} \ h^{-1} \ M_\odot$ to $\lesssim 5\%$, improving on previous results by a factor of 2–3. We derive fitting functions for the halo mass function in this mass range for a wide range of overdensities, both at $z = 0$ and earlier epochs. Earlier studies have sought to calibrate a universal mass function, in the sense that the same functional form and parameters can be used for different cosmologies and redshifts when expressed in appropriate variables. In addition to our fitting formulae, our main finding is that the mass function cannot be represented by a universal function at this level or accuracy. The amplitude of the "universal" function decreases monotonically by $\approx 20\%$–$50\%$, depending on the mass definition, from $z = 0$ to 2.5. We also find evidence for redshift evolution in the overall shape of the mass function.

*Subject headings:* cosmology: theory — large-scale structure of universe — methods: numerical

## 1. INTRODUCTION

Galaxy clusters are observable out to high redshift ($z \lesssim 1$–2), making them a powerful probe of cosmology. The large numbers and high concentration of early type galaxies make clusters bright in optical surveys, and the high intracluster gas temperatures and densities make them detectable in X-ray and through the Sunyaev-Zel'dovich (SZ) effect. The evolution of their abundance and clustering as a function of mass is sensitive to the power spectrum normalization, matter content, and the equation of state of the dark energy and, potentially, its evolution (e.g., Holder et al. 2001; Haiman et al. 2001; Weller et al. 2002; Majumdar & Mohr 2003). In addition, clusters probe the growth of structure in the universe, which provides constraints different from and complementary to the geometric constraints by the supernovae Type Ia (e.g., Albrecht et al. 2006). In particular, the constraints from structure growth may be crucial in distinguishing between the possibilities of the cosmic acceleration driven by dark energy or modification of the magnitude-redshift relation due to the non-GR gravity on the largest scales (e.g., Knox et al. 2006).

The potential and importance of these constraints have motivated current efforts to construct several large surveys of high-redshift clusters using both the ground-based optical and Sunyaev-Zel'dovich (SZ) surveys and X-ray missions in space. In order to realize the full statistical power of these surveys, we must be able to make accurate predictions for abundance evolution as a function of cosmological parameters.

Traditionally, analytic models for halo abundance as a function of mass have been used for estimating expected evolution (Press & Schechter 1974; Bond et al. 1991; Lee & Shandarin 1998; Sheth & Tormen 1999). Such models, while convenient to use, require calibration against cosmological simulations. In addition, they do not capture the entire complexity of halo formation and their ultimate accuracy is likely insufficient for precision cosmological constraints. A precision mass function can most directly be achieved through explicit cosmological simulation.

The standard for precision determination of the mass function from simulations was set by Jenkins et al. (2001) and Evrard et al. (2002), who have presented fitting function for the halo abundance accurate to ~10%–20%. These studies also showed that this function was universal, in the sense that the same function and parameters could be used to predict halo abundance for different redshifts and cosmologies. Warren et al. (2006) have further improved the calibration to ≈5% accuracy for a fixed cosmology at $z = 0$. Several other studies have tested the universality of the mass function at high redshifts (Reed et al. 2003, 2007; Lukic et al. 2007; Cohn & White 2008).

One caveat to all these studies is that the theoretical counts as a function of mass have to be converted to the counts as a function of the cluster properties observable in a given survey. Our understanding of physics that shapes these properties is, however, not sufficiently complete to make reliable, robust predictions. The widely adopted strategy is therefore to calibrate abundance as a function of total halo mass and calibrate the relation between mass and observable cluster properties either separately or within a survey itself using nuisance parameters (e.g., Majumdar & Mohr 2004; Lima & Hu 2004, 2005, 2007). The success of such a strategy, however, depends on how well cluster observables correlate with total cluster mass and whether evolution of this correlation with time is sufficiently simple (e.g., Lima & Hu 2005).

Tight intrinsic correlations between X-ray, SZ, and optical observables and cluster mass are expected theoretically (e.g., Bialek et al. 2001; da Silva et al. 2004; Motl et al. 2005; Nagai 2006; Kravtsov et al. 2006) and were shown to exist observationally

[1] Kavli Institute for Cosmological Physics, University of Chicago, 5640 South Ellis Avenue, Chicago, IL 60637.
[2] Department of Astronomy and Astrophysics, University of Chicago, 5640 South Ellis Avenue, Chicago, IL 60637.
[3] Enrico Fermi Institute, University of Chicago, 5640 South Ellis Avenue, Chicago, IL 60637.
[4] Department of Astronomy, New Mexico State University.
[5] Department of Physics, University of Maryland, College Park.
[6] Theoretical Astrophysics, Los Alamos National Labs.
[7] Grupo de Astrofísica, Universidad Autónoma de Madrid.
[8] Astrophysikalisches Institut Potsdam, Potsdam, Germany.

TABLE 1
Properties of the Simulation Set

| $L_{box}$ ($h^{-1}$ Mpc) | Name | $\epsilon$ ($h^{-1}$ kpc) | $N_p$ | $m_p$ ($h^{-1}$ $M_\odot$) | $(\Omega_m, \Omega_b, \sigma_8, h, n)$ | Code | $z_i$ | $z_{out}$ | $\Delta_{max}$ |
|---|---|---|---|---|---|---|---|---|---|
| 768 | H768 | 25 | $1024^3$ | $3.51 \times 10^{10}$ | (0.3, 0.04, 0.9, 0.7, 1) | HOT | 40 | 0 | 800 |
| 384 | H384 | 14 | $1024^3$ | $4.39 \times 10^{9}$ | (0.3, 0.04, 0.9, 0.7, 1) | HOT | 48 | 0 | 3200 |
| 271 | H271 | 10 | $1024^3$ | $1.54 \times 10^{9}$ | (0.3, 0.04, 0.9, 0.7, 1) | HOT | 51 | 0 | 3200 |
| 192 | H192 | 4.9 | $1024^3$ | $5.89 \times 10^{8}$ | (0.3, 0.04, 0.9, 0.7, 1) | HOT | 54 | 0 | 3200 |
| 96 | H96 | 1.4 | $1024^3$ | $6.86 \times 10^{7}$ | (0.3, 0.04, 0.9, 0.7, 1) | HOT | 65 | 0 | 3200 |
| 1280 | L1280 | 120 | $640^3$ | $5.99 \times 10^{11}$ | (0.27, 0.04, 0.9, 0.7, 1) | GADGET2 | 49 | 0, 0.5, 1.0 | 600 |
| 500 | L500 | 15 | $1024^3 \times 2$ | $8.24 \times 10^{9}$ | (0.3, 0.045, 0.9, 0.7, 1) | GADGET2 | 40 | 0, 0.5, 1.25, 2.5 | 3200 |
| 250 | L250 | 7.6 | $512^3$ | $9.69 \times 10^{9}$ | (0.3, 0.04, 0.9, 0.7, 1) | ART | 49 | 0, 0.5, 1.25, 2.5 | 3200 |
| 120 | L120 | 1.8 | $512^3$ | $1.07 \times 10^{9}$ | (0.3, 0.04, 0.9, 0.7, 1) | ART | 49 | 0, 0.5, 1.25, 2.5 | 3200 |
| 80 | L80 | 1.2 | $512^3$ | $3.18 \times 10^{8}$ | (0.3, 0.04, 0.9, 0.7, 1) | ART | 49 | 0, 0.5, 1.25, 2.5 | 3200 |
| 1000 | L1000W | 30 | $1024^3$ | $6.98 \times 10^{10}$ | (0.27, 0.044, 0.79, 0.7, 0.95) | ART | 60 | 0, 0.5, 1.25, 2.5 | 3200 |
| 500 | L500Wa | 15 | $512^3 \times 2$ | $6.20 \times 10^{10}$ | (0.24, 0.042, 0.75, 0.73, 0.95) | GADGET2 | 40 | 0 | 3200 |
| 500 | L500Wb | 15 | $512^3 \times 2$ | $6.20 \times 10^{10}$ | (0.24, 0.042, 0.75, 0.73, 0.95) | GADGET2 | 40 | 0 | 3200 |
| 500 | L500Wc | 15 | $512^3 \times 2$ | $6.20 \times 10^{10}$ | (0.24, 0.042, 0.8, 0.73, 0.95) | GADGET2 | 40 | 0 | 3200 |
| 384 | H384W | 14 | $1024^3$ | $3.80 \times 10^{9}$ | (0.26, 0.044, 0.75, 0.71, 0.94) | HOT | 35 | 0 | 3200 |
| 384 | H384$\Omega_m$ | 14 | $1024^3$ | $2.92 \times 10^{9}$ | (0.2, 0.04, 0.9, 0.7, 1) | HOT | 42 | 0 | 3200 |
| 120 | L120W | 0.9 | $1024^3$ | $1.21 \times 10^{8}$ | (0.27, 0.044, 0.79, 0.7, 0.95) | ART | 100 | 1.25, 2.5 | 3200 |
| 80 | L80W | 1.2 | $512^3$ | $2.44 \times 10^{8}$ | (0.23, 0.04, 0.75, 0.73, 0.95) | ART | 49 | 0, 0.5, 1.25, 2.5 | 3200 |

Notes.—The top set of 5 simulations are from the Warren et al. (2006) study. The second list of 5 simulations are of the same WMAP1 cosmology, but with different numerical codes. The third list of 8 simulations are of alternate cosmologies, focusing on the WMAP3 parameter set. The HOT code employs Plummer softening, while GADGET employs spline softening. The values of $\epsilon$ listed for the GADGET simulations are the equivalent Plummer softening; when calculating the spline softening kernel, GADGET uses a value of $1.4\epsilon$. The force resolution of the ART code is based on the size of the grid cell at the highest level of refinement. The value $\Delta_{max}$ is the highest overdensity for which the mass function can measured directly. Above this $\Delta$, halo mass are inferred from the rescaling procedure in § 2.3. A graphical key of this table is shown in Figure 1.

(e.g., Mohr et al. 1999; Lin et al. 2004; Vikhlinin et al. 2006; Maughan 2007; Arnaud et al. 2007; Sheldon et al. 2007; Zhang et al. 2008) in the case when both observables and masses are defined within a certain *spherical* radius enclosing a given overdensity. The majority of the mass function calibration studies, however, have calibrated the mass function with halos and masses measured using the friends-of-friends (FOF) percolation algorithm. This algorithm is efficient, straightforward to implement, and is therefore appealing computationally. The FOF algorithm does not assume any geometry for the halo, unlike the enforced sphericity of SO. This is advantageous given that halos have varied shapes. However, the relation between the FOF masses and observables is quite uncertain.

As we show below (see § 2.3 and Fig. 2), there is large, redshift-dependent, and asymmetric scatter between the FOF mass and mass measured within a spherical overdensity, which implies that there is also large asymmetric scatter between the FOF mass and cluster observables. This does not bode well for self-calibration of such relations. Furthermore, there is no way to measure the equivalent of the FOF mass in observations, which means that any calibration of the FOF mass and observables will have to rely on simulations. An additional issue is that halos identified with an FOF algorithm may not have one-to-one correspondence to the objects identified in observational surveys. For example, the FOF finder is known to join neighboring halos into a single object even if their centers are located outside each other's virial radii. Such objects, however, would be identified as separate systems in X-ray and SZ surveys.

Although no halo-finding algorithm applied on simulations containing only dark matter may be perfect in identifying all systems that would be identified in a given observational survey, the spherical overdensity (SO) halo finder, which identifies objects as spherical regions enclosing a certain overdensity around density peaks (Lacey & Cole 1994), has significant benefits over the FOF both theoretically and observationally. Most analytic halo models (see, e.g., Cooray & Sheth 2002, for review) assume that halos are spherical, and the statistics derived are sensitive to the exact halo definition. To be fully self-consistent, the formulae for halo properties, halo abundance, and halo bias, on which the calculations rely, should follow the same definition. The tight correlations between observables and masses defined within spherical apertures means that connecting observed counts to theoretical halo abundances is relatively straightforward and robust. At the same time, the problem of matching halos to observed systems is considerably less acute for halos identified around density peaks, compared to halos identified with the FOF algorithm.

Thus, there is substantial need for a recalibration of the halo mass function based on the SO algorithm for a range of overdensities probed by observations and frequently used in theoretical calculations (∼200–2000). Such calibration for the standard ΛCDM cosmology is the main focus of this paper. Specifically, we focus on accurate calibration of halo abundances for intermediate- and high-mass halos (∼$10^{11}$–$10^{15}$ $h^{-1}$ $M_\odot$) over the range of redshifts ($z \sim 0$–2) most relevant for the current and upcoming large cluster surveys.

The paper is organized as follows. In § 2 we describe our simulation set and SO algorithm. In § 3 we present results for the mass function, demonstrating how our results depend on cosmology and redshift. In § 4 we summarize and discuss our results.

Throughout this paper *we use masses defined within radii enclosing a given overdensity with respect to the mean density of the universe at the epoch of analysis.*

## 2. METHODS

### 2.1. *Simulation Set*

Table 1 lists our set of simulations. All the simulations are based on variants of the flat, ΛCDM cosmology. The cosmological
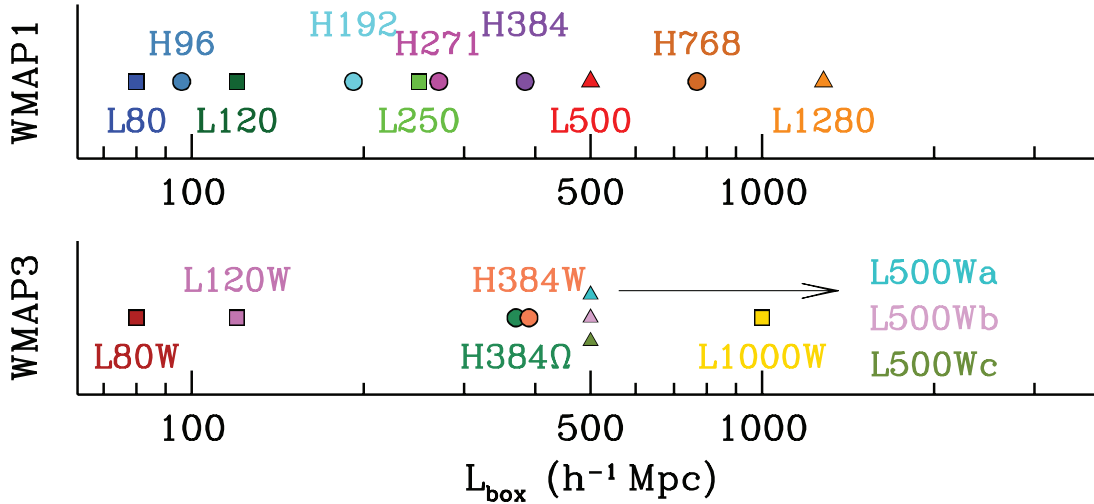
FIG. 1.—Graphical key for the list of simulations in Table 1. *Top*: Point styles for all the WMAP1 simulations ordered by the box size. Each simulation is represented with a different color, while different point types represent different numerical codes: HOT (*circles*), ART (*squares*), GADGET2 (*triangles*). *Bottom*: All WMAP3 simulations, as well as H384Ω, the low-Ω_m simulation. See Table 1 for the details of each simulation.

parameters for the majority of the simulations reflect the zeitgeist of the first-year *WMAP* results (Spergel et al. 2003). We will refer to this cosmology as WMAP1. A smaller number of simulations have cosmological parameters closer to the three-year *WMAP* constraints (Spergel et al. 2007), in which both $\Omega_m$ and $\sigma_8$ are lower and the initial power spectrum contains significant tilt of $n = 0.95$. This subset of simulations are not of the same identical parameter set, but rather represent slight variations around a parameter set we will refer to globally as WMAP3.

The largest simulation by volume followed a cubic box of $1280\,h^{-1}$ Mpc size. There are 50 realizations of this simulation performed with the GADGET2 code (Springel 2005), which have been kindly provided to us by R. Scoccimarro (2008, private communication). With the exception of these $1280\,h^{-1}$ Mpc boxes, the initial conditions for all simulations were created using the standard first-order Zel'dovich approximation (ZA). Crocce et al. (2006) point out possible systematic errors in the resulting mass function if first-order initial conditions are started insufficiently early. Using second-order Lagrange perturbation theory (2LPT) to create initial conditions, they identify discrepancies between the halo mass function from their simulations and that of Warren et al. (2006) at the highest masses. In Warren et al. (2006) several boxes larger than $768\,h^{-1}$ Mpc were utilized in the analysis that are not listed in Table 1. In tests with our spherical overdensity halo finder, we find a discrepancy between the 2LPT simulations and these simulations. At this point, it is not yet clear whether the discrepancy is due to the effect advocated by Crocce et al. (2006) or due to other numerical effects. We explore the issue of initial starting redshift in some detail in the Appendix A. What is clear, however, is that results of these simulations systematically deviate from other higher resolution simulations, especially for larger values of overdensities. We therefore do not include them in our analyses.

The first five simulations listed in Table 1 were used in Warren et al. (2006) in their analyses. The integrations were performed with the hashed oct-tree (HOT) code of Warren & Salmon (1993). In addition, there are two HOT simulations in the WMAP3 parameter set. These simulations will be referred to in the text by their box size, in $h^{-1}$ Mpc, prefixed by the letter "H." Simulations in the WMAP3 set will be appended with the letter "W." Due to identical box sizes between parameter sets, H384 will refer to the WMAP1 simulation, H384W will refer to the simulation with WMAP3 parameters, and H384Ω will refer to the

low-$\Omega_m$ simulation (which we will include in the WMAP3 simulation subset).

There are six simulations using the adaptive refinement technique (ART) of Kravtsov et al. (1997) and four that use GADGET2 in addition to the L1280 realizations. The L80 and L120 ART boxes modeling the WMAP1 cosmology are described in Kravtsov et al. (2004) and L250 simulation is described by A. Tasitsiomi et al. (2008, in preparation), while the three WMAP3 boxes are presented here. The L500 simulations are described in Gottlöber & Yepes (2007) and Yepes et al. (2007).[9] These simulations contain equal numbers of dark matter and SPH gas particles (without cooling). The ART and GADGET2 simulations will be referred by their box size with prefix "L." WMAP3 simulations have a "W" as a suffix.

Our simulation set comprises three different *N*-body codes, one based on the popular tree algorithm (HOT), one based on grid codes with small-scale refinement of high-density regions (ART), and one that combines grid and tree algorithms (GADGET2). We present a key in Figure 1 that graphically displays the range of box sizes. Each simulation is represented by a different color, while different point types refer to different simulation codes: circles for HOT, squares for ART, and triangles for GADGET2. These point symbols and colors will be used consistently in the figures below.

## 2.2. *Halo Identification*

The standard spherical overdensity algorithm is described in detail in Lacey & Cole (1994). However, in our approach we have made several important modifications. In Lacey & Cole (1994) the centers of halos are located on the center of mass of the particles within the sphere. Due to substructure, this center may be displaced from the main peak in the density field. Observational techniques such as X-ray cluster identification locate the center of the halo at the peak of the X-ray flux (and therefore the peak of density of the hot intracluster gas). Optical cluster searches will often locate the cluster center at the location of the brightest member, which is also expected to be located near the peak of X-ray emission (Lin et al. 2004; Koester et al. 2007; Rykoff et al. 2008). Thus, we locate the centers of halos at their density peaks.

---

[9] See also http://astro.ft.uam.es/marenostrum/universe/index.html.

Our halo finder begins by estimating the local density around each particle within a fixed top-hat aperture with radius approximately 3 times the force softening of each simulation. Beginning with the highest density particle, a sphere is grown around the particle until the mean interior density is equal to the input value of $\Delta$, where $\Delta$ is the overdensity within a sphere of radius $R_\Delta$ with respect to the mean density of the universe at the epoch of analysis, $\bar{\rho}_m(z) \equiv \Omega_m(z)\rho_{\rm crit}(z) = \bar{\rho}_m(0)(1 + z)^3$:

$$\Delta = \frac{M_\Delta}{(4/3)\pi R_\Delta^3 \bar{\rho}_m}. \qquad (1)$$

All values of $\Delta$ listed in this paper are with respect to $\bar{\rho}_m(z)$.

Since local densities smoothed with a top-hat kernel are somewhat noisy, we refine the location of the peak of the halo density with an iterative procedure. Starting with a radius of $r = R_\Delta/3$, the center of mass of the halo is calculated iteratively until convergence. The value of $r$ is reduced iteratively by 1%, and the new center of mass found until a final smoothing radius of $R_\Delta/15$, or until only 20 particles are found within the smoothing radius. At this small aperture, the center of mass corresponds well to the highest density peak of the halo. This process is computationally efficient and both eliminates noise and accounts for the possibility that the chosen initial halo location resides at the center of a large substructure; in the latter case, the halo center will wander toward the larger mass and eventually settle on its center. Once the new halo center is determined, the sphere is regrown and the mass is determined.

All particles within $R_\Delta$ are marked as members of a halo and skipped when encountered in the loop over all particle densities. Particles located just outside of a halo can be chosen as candidate centers for other halos, but the iterative halo-centering procedure will wander into the parent halo. Whenever two halos have centers that are within the larger halo's $R_\Delta$, the halo with the largest maximum circular velocity, defined as the maximum of the circular velocity profile, $V_c(r) = [GM(<r)/r]^{1/2}$, is taken to be the parent halo and the other halo is discarded.

We allow halos to overlap. As long as the halo center does not reside within $R_\Delta$ of another halo, the algorithm identifies these objects as distinct structures. This is in accord with X-ray or SZ observations which would identify and count such objects as separate systems. The overlapping volume may contain particles. Rather than attempt to determine which halo each particle belongs to, or to divide each particle between the halos, the mass is double counted. No solution to this problem is ideal, but we find that the total amount of double-counted mass is only $\sim$0.75% of all the mass located within halos, with no dependence on halo mass. This parallels the treatment of close pairs of clusters detected observationally. When two X-ray clusters are found to have overlapping isophotal contours, each system is treated individually and double counting of mass will occur as well.

For each value of $\Delta$, the halo finder is run independently. Halo mass functions are binned in bins of width 0.1 in $\log M$ with no smoothing. Errors on each mass function are obtained by the jackknife method; each simulation is divided into octants and the error on each mass bin is obtained through the variance of the halo number counts as each octant is removed from the full simulation volume (e.g., Zehavi et al. 2005, eq. [6]). The jackknife errors provide a robust estimate of both the cosmic variance, which dominates at low masses, and the Poisson noise that dominates at high masses (see Hu & Kravtsov [2003] for a relative contributions of each source of error as a function of halo mass).

When fitting the data, we only use data points with error bars less than 25% to reduce noise in the fitting process. We note that

mass bins will be correlated (low-mass bins more so than high-mass ones). We do not calculate the full covariance matrix of each mass function, so the $\chi^2$ values obtained from the fitting procedure should be taken as a general guide of goodness of fit, but not as an accurate statistical measure. However, we note that the data from multiple simulations in each mass range will be uncorrelated, and the lack of a covariance matrix should not bias our best-fit values for the mass function.

### 2.3. Comparison of FOF and SO halos

Cole & Lacey (1996) and later White (2001, 2002) demonstrated that there is scatter between the masses of halos identified with the FOF and SO halo definitions, as well as an offset between the mean halo masses using the canonical values of the linking length $l = 0.2$ in the FOF algorithm and overdensity $\Delta = 200$ in the SO approach. Figure 2 compares the masses of halos identified with these two definitions for three different simulations. Halos in a simulation are first identified with our SO approach, then the FOF finder is subsequently run, beginning at the center of the SO halo. Figure 2a compares $\Delta = 200$ to $l = 0.2$. The symbols represent the median mass ratio $r_M = M_{200}/M_{\rm FOF.2}$ as a function of $M_{200}$. The curves represent the upper and lower 90% bounds on the distribution of mass ratios. Although the median is near unity, the scatter is large and highly asymmetric.

The asymmetry in the distribution is due to the FOF algorithm linking two or more distinct objects in close proximity to each other. Because we allow halos to overlap, FOF will treat these halos as a single object. Due to the arbitrary shape of FOF halos, the algorithm also links SO objects that do not overlap. The median mass ratio is also sensitive to the number of particles per halo; FOF halos are known to be biased toward higher masses at low particle number (Warren et al. 2006). This occurs because the linking length becomes comparable to the density scale length at the outskirts of low-$N$ halos. The scatter between mass definitions is not alleviated by making the linking length smaller. This is shown in Figure 2b, in which the same results are shown for $\Delta = 1600$ and $l = 0.1$. The median is once again near unity, and the scatter remains identical. We note also that there is an offset in the median between simulations as well; the results from L1000W are $\sim$ 5% lower than the other simulations at $l = 0.2$ and $\sim$10% lower at $l = 0.1$. This offset is not due to the change in cosmology between the L1000W and the other simulations; therefore, it must be a result of the lower mass resolution.

We find that the curvature in the median mass ratio is alleviated when adjusting the masses $M_{\rm FOF.2}$ by the Warren et al. (2006) correction formula, $(1 - N_p^{-0.6})$, where $N_p$ is the number of particles in a halo. However, the curvature is not entirely ameliorated by this formula at $l = 0.1$, demonstrating that the mass errors in FOF halos depend on the linking length. We find that $(1 - N_p^{-0.5})$ is sufficient to remove the FOF bias for $l = 0.1$. Figures 2c and 2d show the distribution of mass ratios for halos between $10^{13}$ and $10^{14}\,h^{-1}\,M_\odot$ for one of the simulations. The solid histograms present results at $z = 0$ and the dotted histograms is for $z = 1.25$. Both the $z = 0$ histograms exhibit a large, constant tail to low ratios. At higher redshift, the asymmetry of $P(r_M)$ becomes even stronger. The correlation between spherically defined masses and the FOF masses is thus broad and evolves with redshift.

Within the $z = 0.5$ output of the L1000W simulation, we find 21% more $M > 10^{14}\,h^{-1}\,M_\odot$ $l = 0.2$ FOF halos than $\Delta = 200$ objects at the same mass cut. Predicting the abundance of higher overdensity objects using $l = 0.2$ FOF objects leads to larger errors. A simple rescaling of the masses of the FOF halos to $\Delta = 1600$ by assuming Navarro-Frenk-White (NFW) density profiles (see the discussion in § 2.4) leads to an overprediction of
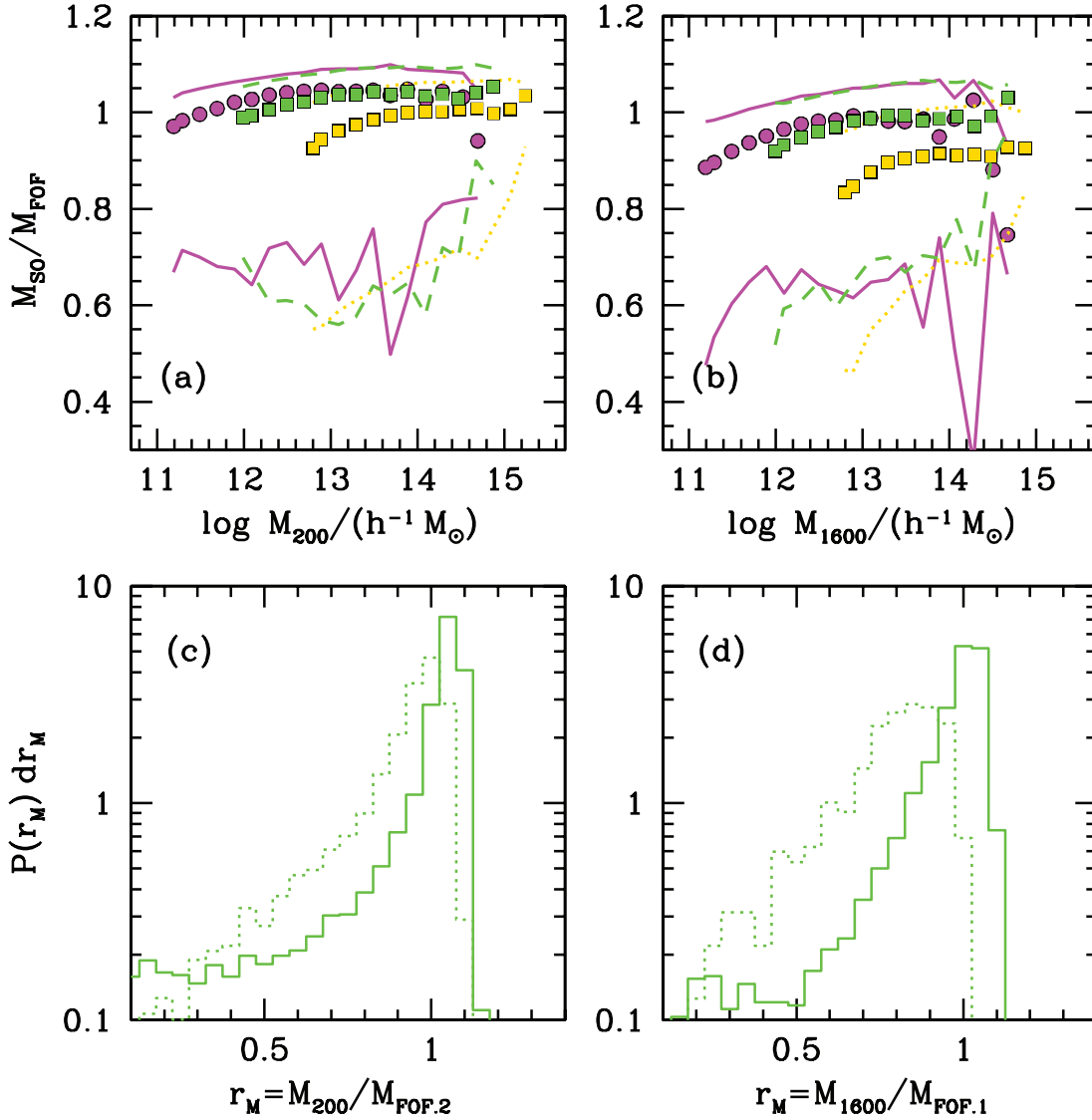
FIG. 2.—Comparison between spherical overdensity masses and friends-of-friends masses for the same sample of objects from H384, L250, and L1000W. (*a*) Comparison of the masses of $\Delta = 200$ halos to FOF halos with $l = 0.2$. The symbols represent the median mass ratio, for objects binned by $M_{200}$. The curves show the upper 90% and lower 10% bounds of the distribution of mass ratios in each $M_{200}$ bin: solid line for H384, dashed line for L250, and dotted line for L1000W. The asymmetry in the mass ratio distribution reflects the tendency of FOF to link objects together. (*b*) Comparison of $\Delta = 1600$ halos to FOF objects with $l = 0.1$. (*c*) Distribution of mass ratios, $r_M = M_{200}/M_{FOF.2}$, for halos $13 \leq \log M_{200} \leq 14$ (*solid line*). The long tail of the distribution at $r_M < 0.5$ indicates SO halos that are linked with other virialized objects in the FOF halo-finding process. The dotted line is the same distribution at $z = 1.25$. (*d*) Distribution of $r_M$ for the same mass range, for the $\Delta = 1600$ and FOF linking length $l = 0.1$. Solid and dotted lines are $z = 0$ and 1.25, respectively. Both (*c*) and (*d*) show results for the L250 run.

the number of objects of $M > 10^{14}\, h^{-1}\, M_\odot$ by ~80%. These discrepancies become larger for higher redshifts, higher halo mass thresholds, and higher overdensities.

This has significant implications for comparisons with observational cluster counts. Given that cluster observables correlate strongly with the spherical overdensity masses, the large scatter between $M_\Delta$ and $M_{FOF}$ indicates that the FOF correlation will be weaker. If one is to use a halo mass function calibrated against halos and masses identified with the FOF algorithm, a significant additional effort would be required to calibrate the scatter between FOF masses and observables as a function of redshift, mass, and cosmology. In addition, this calibration will have to rely solely on theoretical modeling, because the mass equivalent to the FOF cannot be directly measured in observations. The use of the halo abundance predictions made with the spherical overdensity algorithm is therefore strongly preferred.

### 2.4. *Accounting for Effects of Resolution*

Defining the halo masses within a radius enclosing a given overdensity stipulates that the halo mass is the integrated density profile within a fixed radius. This means that the mass depends on the internal density distribution of the halo and is thus more susceptible to the effects of resolution. The FOF masses, on the other hand, are measured within a given isodensity surface and are therefore less sensitive to the internal mass distribution. For example, Lukic et al. (2007) demonstrate that a reasonable FOF mass function can be obtained through a low-resolution simulation with as little as eight time steps. If the same simulation is performed twice with different resolutions, the same density peak in the lower resolution simulation will have a shallower density profile and will in general have a different measured mass, $M_\Delta$. The result is a systematic artificial shift in the estimated halo mass
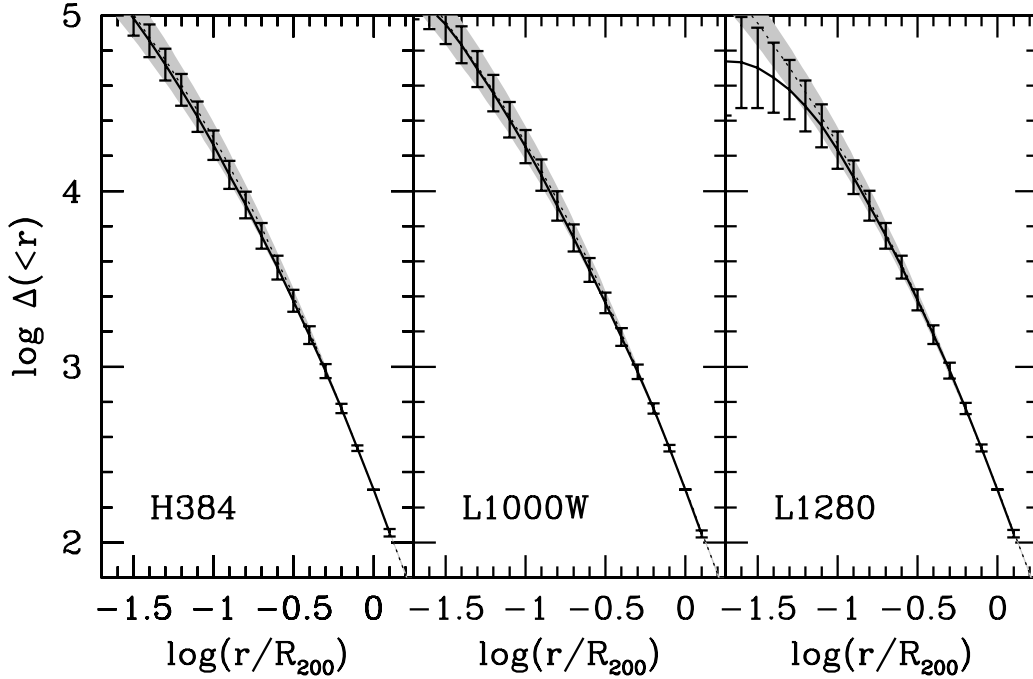
Fig. 3.—Halo density profiles are compared to analytic predictions for three different simulations. In each panel, the dotted curve represents the mean interior density given by an NFW profile with $c(M)$ from Dolag et al. (2004). The shaded region is the expected scatter assuming $\sigma_{\log c} = 0.12$. The solid curves with error bars represent the numerical results. *Left*: Results from H384 for all halos $M > 10^{14.5} \, h^{-1} \, M_\odot$. *Center and right*: Results for halos $M > 10^{15} \, h^{-1} \, M_\odot$. The center and left panel demonstrate that halo profiles are well resolved in these simulations. *Right*: Significant deviations from the expected NFW profile at $r < 0.1 R_{200}$ in the lower resolution L1280 simulation.

function. This effect will be larger for larger values of $\Delta$; as the radius $R_\Delta$ of a halo becomes smaller, the finite force resolution of the simulation will have a larger impact on the inferred mass.

To measure the SO mass function reliably at high $\Delta$, we test whether the halo density profiles are properly resolved in each of the analyzed simulations at the overdensity in question. Figure 3 illustrates one of the resolution tests that we performed. It compares the halo density profiles from simulations to the expected profiles. For the latter we use the well-tested Navarro et al. (1997) profile with the concentration for a given mass measured in high-resolution simulations by Dolag et al. (2004)[10] and a scatter in concentration of 0.12 in $\log c$. In this figure we show examples of one HOT simulation (H384), one ART simulation (L1000W), and one GADGET2 simulation (L1280). The HOT and ART simulations have force resolutions of 14 and 30 $h^{-1}$ kpc, respectively, which is well within the scale radius of a typical cluster-sized halo. The results for both the mean profile and its scatter are in excellent agreement with the NFW profile. The L1280 simulation has a force resolution of 120 $h^{-1}$ kpc, and deviations from the expected profile become clear at $r < 0.1 R_{200}$. These differences will propagate into the estimate of the mass function if they are not taken into account.

The results of comparisons similar to those shown in Figure 3 clearly identify which radii and which simulations profiles are affected by resolution. These results can then be used to determine the range of overdensities for which masses can be measured reliably in a given simulation. This is illustrated in Figure 4, which shows the mass functions from three different simulations at four values of $\Delta$. The mass functions are plotted relative to the best-fit mass functions at each $\Delta$, which are described in more detail

below in § 3. At each overdensity we compare the mass functions measured in simulations to mass functions obtained by taking the individual halos found using the SO halo finder with $\Delta = 200$ and rescaling their masses assuming the NFW profile, taking into account scatter in concentrations (see, e.g., White 2001; Hu & Kravtsov 2003). We use the concentration-mass relation and scatter measured directly from our simulations (J. Tinker et al., in preparation). The figure shows that the measured and rescaled mass functions are in good agreement for $\Delta \leq 800$, where the scaled-up mass function is ~5% higher than the true mass function. This error is accrued from the halos located within $R_{200}$, which can become separate halos for higher overdensities and are not accounted for in the rescaling process.

At higher overdensities, the agreement is markedly worse, especially for the lower resolution L1280 boxes. At $\Delta = 1600$, the measured mass function is underestimated by ~10%, increasing to ~20% at $\Delta = 3200$. Therefore, for this simulation we use the directly measured mass function only at $\Delta \leq 600$, while at higher $\Delta$ we calculate the mass function by mass rescaling using halos identified with an overdensity $\Delta = 600$. A scaling baseline of $\log(\Delta_{high}/\Delta_{low}) \leq 0.9$ accrues only $\lesssim 2\%$ error in the amplitude of the mass function at these masses. Thus, the rescaled halo catalogs are reliable for calibrating the halo mass function at high overdensity. This procedure is used to measure high-$\Delta$ mass functions for L768 (for $\Delta > 800$) and L1280 (for $\Delta > 600$).

At $\Delta = 200$ we choose a conservative minimum value of no less than 400 particles per halo. Below this value resolution effects become apparent, and simulations with differing mass resolutions begin to diverge. This is readily seen in the SO mass functions analyzed in Jenkins et al. (2001). At higher $\Delta$, halos are probed at significantly smaller radii, and the resolution requirements are more stringent. Thus at higher $\Delta$ we increase the minimum number of particles such that, at $\Delta = 3200$, $N_{min}$ is higher by a factor of 4. Exact values for each overdensity are listed in Table 2.

[10] $c_{200}(M) = 9.59 \times (M/10^{14})^{-0.102}$, normalized to the WMAP1 cosmology. When changing cosmology, we shift the normalization using the fractional change in concentration from the Bullock et al. (2001) model at $M = 10^{13} \, h^{-1} \, M_\odot$.
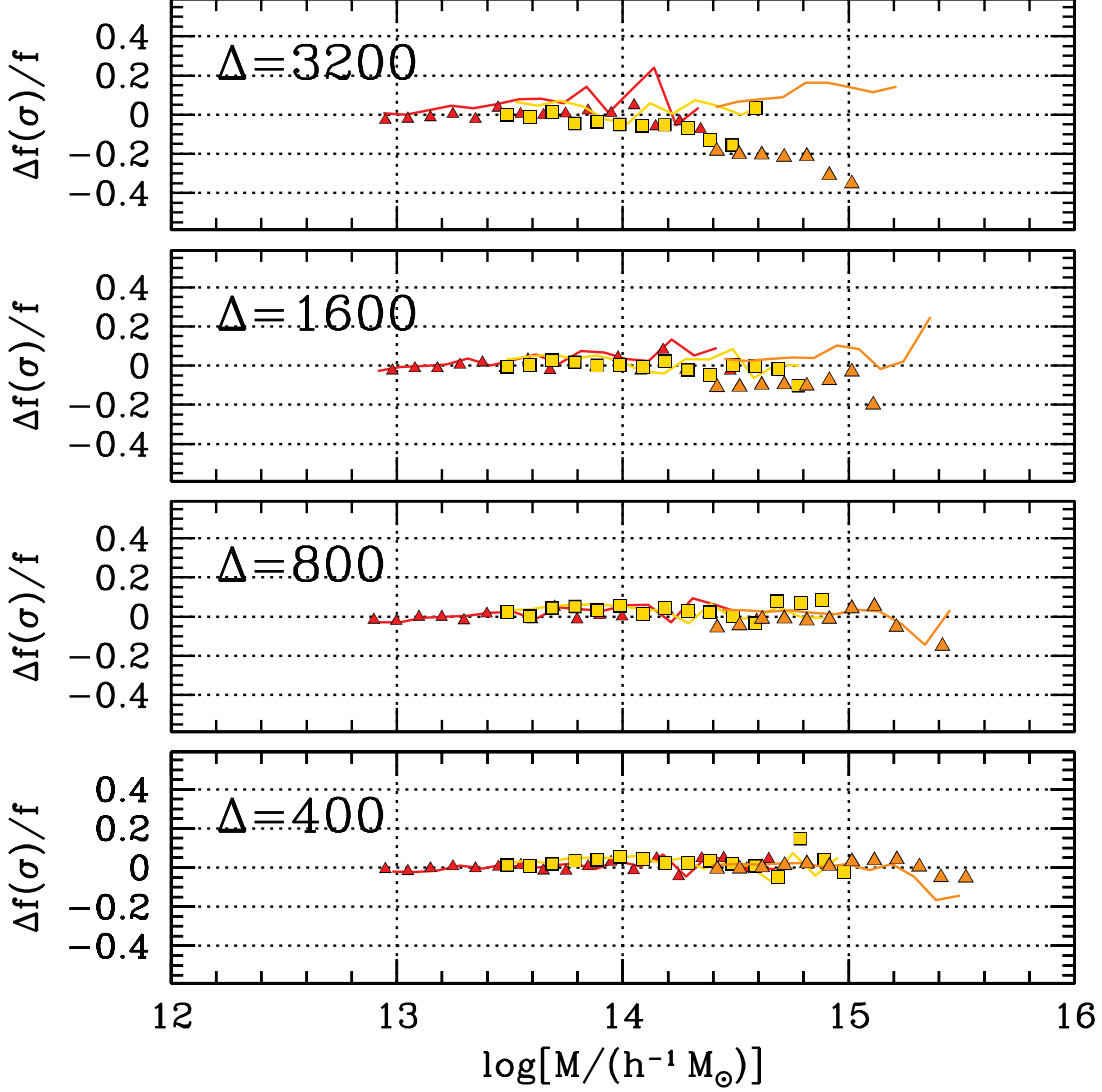
FIG. 4.—Test of the resolution of the large-volume simulations, L500, L1000W, and one realization of L1280. In each panel, the mass functions are plotted as residuals with respect to the best-fit $f(\sigma)$ function from Table 2. The symbols represent the mass functions measured directly from the simulations at each $\Delta$. The curves are mass functions inferred from the $\Delta = 200$ halo catalog of each simulation, where the mass of each $\Delta = 200$ halo is scaled to higher overdensities assuming an analytic NFW halo (including scatter in concentrations at fixed mass). For the two higher resolution simulations, the scaled and true mass function are in agreement. Due to insufficient resolution, the L1280 mass function falls below the scaled mass function at high $\Delta$.

TABLE 2
MASS FUNCTION PARAMETERS FOR $f(\sigma)$ AT $z = 0$

| $\Delta$ (1) | $A$ (2) | $a$ (3) | $b$ (4) | $c$ (5) | $\chi^2/\nu$ (ALL) (6) | $N_{min}$ (7) | $\chi^2/\nu$ (WMAP1) (8) | $\chi^2/\nu$ (WMAP3) (9) | $\chi^2/\nu$ (WMAP3 fit) (10) |
|---|---|---|---|---|---|---|---|---|---|
| 200.......................... | 0.186 | 1.47 | 2.57 | 1.19 | 1.15 | 400 | 1.07 | 1.66 | 1.62 |
| 300.......................... | 0.200 | 1.52 | 2.25 | 1.27 | 1.17 | 400 | 1.08 | 1.65 | 1.60 |
| 400.......................... | 0.212 | 1.56 | 2.05 | 1.34 | 1.05 | 600 | 0.96 | 1.49 | 1.37 |
| 600.......................... | 0.218 | 1.61 | 1.87 | 1.45 | 1.06 | 600 | 0.99 | 1.55 | 1.28 |
| 800.......................... | 0.248 | 1.87 | 1.59 | 1.58 | 1.10 | 1000 | 1.07 | 1.36 | 1.14 |
| 1200........................ | 0.255 | 2.13 | 1.51 | 1.80 | 1.00 | 1000 | 0.97 | 1.22 | 1.16 |
| 1600........................ | 0.260 | 2.30 | 1.46 | 1.97 | 1.07 | 1600 | 1.03 | 1.34 | 1.25 |
| 2400........................ | 0.260 | 2.53 | 1.44 | 2.24 | 1.11 | 1600 | 1.07 | 1.50 | 1.26 |
| 3200........................ | 0.260 | 2.66 | 1.41 | 2.44 | 1.14 | 1600 | 1.09 | 1.61 | 1.33 |

NOTES.—The value $N_{min}$ is the minimum number of particles per halo used in the fit. Fits are for simulations at $z = 0$. The WMAP1 and WMAP3 $\chi^2/\nu$ values are with respect to the WMAP1 and WMAP3 simulations, respectively, but using the best-fit parameters. The WMAP3 fit $\chi^2/\nu$ values are independent fits using only the WMAP3 simulations.

## 3. HALO MASS FUNCTION

### 3.1. *Fitting Formula and General Results*

Although the number density of collapsed halos of a given mass depends sensitively on the shape and amplitude of the power spectrum, successful analytical *Ansätze* predict the halo abundance quite accurately by using a universal function describing the mass fraction of matter in peaks of a given height, $\nu \equiv \delta_c/\sigma(M, z)$, in the linear density field smoothed at some scale $R = (3M/4\pi\bar{\rho}_m)^{1/3}$ (Press & Schechter 1974; Bond et al. 1991; Sheth & Tormen 1999). Here, $\delta_c \approx 1.69$ is a constant corresponding to the critical linear overdensity for collapse and $\sigma(M, z)$ is the rms variance of the linear density field smoothed on scale $R(M)$. The traditional nonlinear mass scale $M_*$ corresponds to $\sigma = \delta_c$. This fact has motivated the search for accurate universal functions describing simulation results by Jenkins et al. (2001), White (2002), and Warren et al. (2006). Following these studies, we choose the following functional form to describe halo abundance in our simulations:

$$\frac{dn}{dM} = f(\sigma)\frac{\bar{\rho}_m}{M}\frac{d\ln\sigma^{-1}}{dM}. \quad (2)$$

In extended Press-Schechter theory, the overdensity at a location in a linear density field follows a random walk with decreasing smoothing scale. The function $f(\sigma)$ is the $\sigma$-weighted distribution of first crossings of these random walks across a barrier separating collapsed objects from uncollapsed regions (e.g., where the random-walking overdensity first crosses $\delta_c$). The function $f(\sigma)$ is expected to be universal to the changes in redshift and cosmology and is parameterized as

$$f(\sigma) = A\left[\left(\frac{\sigma}{b}\right)^{-a} + 1\right]e^{-c/\sigma^2}, \quad (3)$$

where

$$\sigma^2 = \int P(k)\hat{W}(kR)k^2\,dk, \quad (4)$$

$P(k)$ is the linear matter power spectrum as a function of wavenumber $k$, and $\hat{W}$ is the Fourier transform of the real-space top-hat window function of radius $R$. It is convenient to recall that the matter variance monotonically decreases with increasing smoothing scale; thus, higher $M$ corresponds to lower $\sigma$. In the figures and text, we will use $\log\sigma^{-1}$ as the independent variable. This quantity increases monotonically with halo mass.

The functional form (3) was used in Warren et al. (2006) with minor algebraic difference, and is similar to the forms used by Sheth & Tormen (1999)[11] and Jenkins et al. (2001). Parameters $A$, $a$, $b$, and $c$ are constants to be calibrated by simulations. The parameter $A$ sets the overall amplitude of the mass function, while $a$ and $b$ set the slope and amplitude of the low-mass power law, respectively. The parameter $c$ determines the cutoff scale at which the abundance of halos exponentially decreases.

The best-fit values of these parameters were determined by fitting equation (3) to all the $z = 0$ simulations using $\chi^2$ minimization and are listed in Table 2 for each value of $\Delta$. For $\Delta \geq 1600$,

---

[11] A convenient property of the Sheth & Tormen mass function is that one recovers the mean matter density of the universe when integrating over all mass; the function is normalized such that $\int f(\sigma)\,d\ln\sigma^{-1} = 1$. Eq. (3) does not converge when integrating to $\log\sigma^{-1} = -\infty$. In Appendix C we present a modified fitting function that is properly normalized at all $\Delta$ but still produces accurate results at $z = 0$.
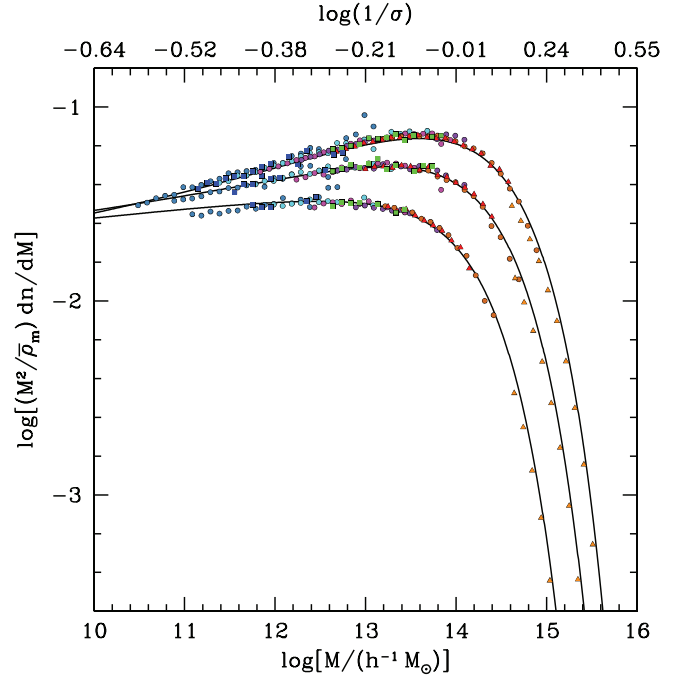


Fig. 5.—Measured mass functions for all WMAP1 simulations, plotted as $(M^2/\bar{\rho}_m)\,dn/dM$ against $\log M$. The solid curves are the best-fit functions from Table 2. The three sets of points show results for $\Delta = 200$, 800, and 3200 ( *from top to bottom* ). To provide a rough scaling between $M$ and $\sigma^{-1}$, the top axis of the plot shows $\sigma^{-1}$ for this mass range for the WMAP1 cosmology. The slight offset between the L1280 results and the solid curves is due to the slightly lower value of $\Omega_m = 0.27$.

we fix the value of $A$ to be 0.26 without any loss of accuracy.[12] This allows the other parameters to vary monotonically with $\Delta$, allowing for smooth interpolation between values of $\Delta$.

Figure 5 shows the mass function measured for three values of $\Delta$ and the corresponding best-fit analytic functions. We plot $(M^2/\bar{\rho}_m)\,dn/dM$ rather than $dn/dM$ to reduce the dynamic range of the $y$-axis, as $dn/dM$ values span nearly 14 orders of magnitude. The figure shows that as $\Delta$ increases the halo masses become systematically smaller. Thus, from $\Delta = 200$ to 3200, the mass scale of the exponential cutoff reduces substantially. The shape of the mass function is also altered; at $\Delta = 200$ the logarithmic slope at low masses is $\sim -1.85$, while at $\Delta = 3200$ the slope is nearly $-2$. This change in slope is due to two effects. First, the fractional change in mass when converting between values of $\Delta$ is not a constant; it depends on halo mass. Because halo concentrations are higher for smaller halos, the fractional change is higher at lower masses, thus steepening the mass function. Second, a number of low-mass objects within $R_{200}$ of a larger halo are "exposed" as distinct halos when halos are identified with $\Delta = 3200$. Although all halos contain substructure, these "revealed" subhalos will only impact overall abundance of objects at low mass, $M \lesssim 10^{12}\,h^{-1}\,M_\odot$, because the satellite fraction (the fraction of all halos located within virial radii of larger halos) decreases rapidly from $\approx 20\%$ to zero for $M > 10^{12}\,h^{-1}\,M_\odot$ (e.g., Kravtsov et al. 2004). This trend can be understood using average properties of subhalos in parent CDM halos. Subhalo populations are approximately self-similar with only a weak trend with mass (e.g., Moore et al. 1999; Gao et al. 2004), and the largest

---

[12] Although a four-parameter function is required to accurately fit the data at low $\Delta$, at high overdensities the error bars are sufficiently large that a degeneracy between $A$ and $a$ emerges, and the data can be fit with only three free parameters, given a reasonable choice for $A$.
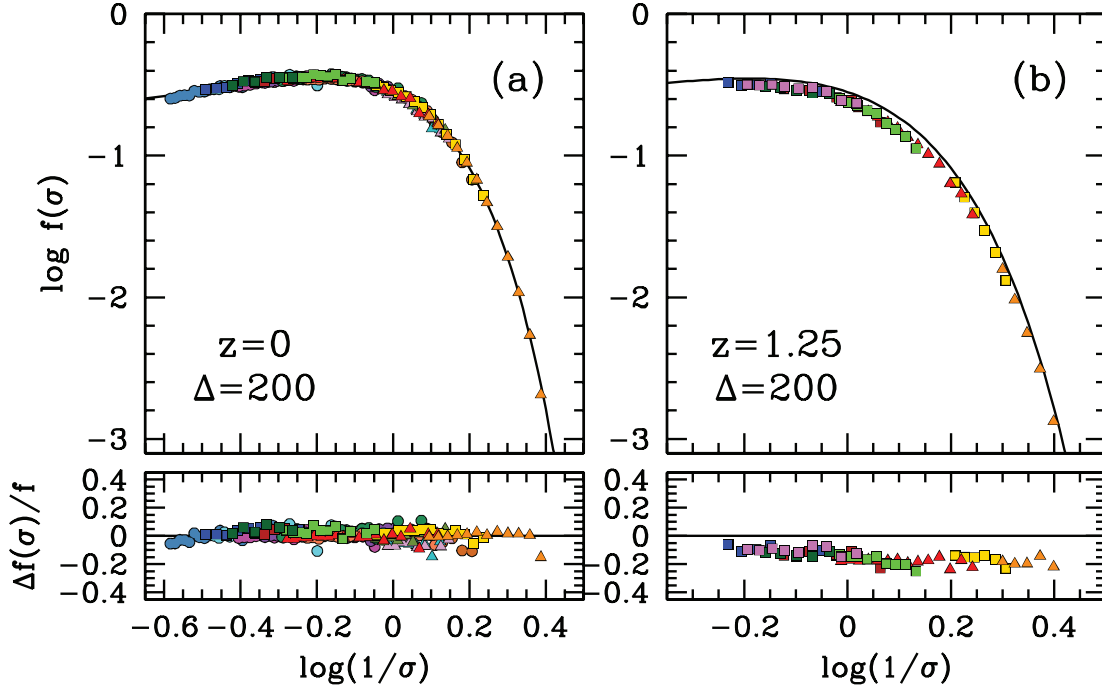
Fig. 6.—(a) Measured $f(\sigma)$ from all simulations in Table 1. Results are presented at $z = 0$ and for $\Delta = 200$. The solid line is the best-fit function of eq. (3). The lower window shows the percentage residuals with respect to the fitting function. In the WMAP1 cosmology, the range on the data points on the $x$-axis is roughly $10^{10.5}$ to $10^{15.5}\,h^{-1}\,M_\odot$. (b) Measured $f(\sigma)$ at $z = 1.25$. We restrict results to simulations for which we have previous redshift outputs. In the WMAP1 cosmology, the range of data points on the $x$-axis is $10^{11}$ to $10^{15}\,h^{-1}\,M_\odot$. The solid line is the same as in (a), which was calibrated at $z = 0$. The lower window shows that the $z = 1.25$ mass function is offset by $\sim20\%$ with respect to the results at $z = 0$.

subhalo typically has a mass of $\approx5\%$–$10\%$ of the host mass. Thus, at a given mass $M$ only hosts with masses $>10M$ can produce significant number of new halos when halo identification at higher $\Delta$ is performed. At high masses, the number of such halos decreases exponentially with mass, and therefore the contribution of such "exposed" halos becomes small.

Figure 6a shows the function $f(\sigma)$ measured for all simulations in Table 1 at $z = 0$ with $\Delta = 200$. The solid curve is equation (3) using the best-fit parameters from Table 2. The residuals with respect to this fit demonstrate the high accuracy of our numerical results and the consistency of different codes, mass resolutions, and cosmologies. Figure 6b shows $f(\sigma)$ at $z = 1.25$ for a subset of simulations for which higher redshift outputs are available. The solid curve represents the results from $z = 0$. At this redshift, the results at $\sim20\%$ below the $z = 0$ results, nearly independent of $\log\sigma^{-1}$. This demonstrates that the mass function is *not* universal in redshift, or for correspondingly large changes in cosmology,[13] at this level of accuracy. We address evolution of $f(\sigma)$ with $z$ in § 3.3 below.

### 3.2. Results as a Function of $\Delta$

The best-fit parameters of equation (3) resulting from fits to *all* simulations for nine values of overdensity are listed in Table 2. Figure 7 shows the residuals of individual WMAP1 simulations with respect to global fits at different $\Delta$. We include L1000W in these plots to show consistency between cosmologies at cluster masses. For the 50 realizations of L1280, we plot the mean $f(\sigma)$ and the error in the mean. Each panel shows the fractional residuals of the measured mass functions with respect to the best-fit $f(\sigma)$ for four values of $\Delta$. To avoid crowding, error bars are plotted for the maximum and minimum mass scale for every simu-

---

[13] Note that we can interpret higher redshift outputs of a given simulation as the $z = 0$ epoch of a simulation with different cosmological parameters corresponding to $\Omega_m(z)$ and other parameters at the redshift in question.

lation; the latter is representative of the cosmic variance given the finite simulation volume, while the former is dominated by Poisson noise. We list formal values of $\chi^2/\nu$ for our diagonal error bars in Table 2. The values in column (6) are for all $z = 0$ simulations, while the value in column (8) is the $\chi^2/\nu$ for the same parameters but with respect to the WMAP1 simulations only. Not surprisingly, the $\chi^2/\nu$ values reduce slightly when comparing the best-fit $f(\sigma)$ to the WMAP1 simulations only, which comprise a majority of the simulations and therefore drive the fitting results.

The solid blue curve in the $\Delta = 200$ panel represents the fitting function of Jenkins et al. (2001) calibrated on their set of $\tau$CDM simulations (their eq. [B3]), using $\Delta = 180$ (rescaling this equation to 200 yields nearly indistinguishable results). At $M \gtrsim 10^{12}\,h^{-1}\,M_\odot$, the Jenkins result is $10\%$–$15\%$ below our results. The Sheth & Tormen (1999) function is similarly offset from our results. In the $\Delta = 400$ panel, the blue curve shows the Jenkins et al. fitting function calibrated to $\Delta = 324$ on their set of $\Lambda$CDM simulations (essentially the WMAP1 cosmology). For this comparison the Jenkins formula has been rescaled to $\Delta = 400$ using the same halo rescaling techniques discussed in § 2.3 and in Hu & Kravtsov (2003). The Jenkins SO(324) function (their eq. [B4]) is in good agreement with our results for $M < 10^{13}\,h^{-1}\,M_\odot$, while at higher masses there are variations of $\pm5\%$–$10\%$.

The solid curves in the $\Delta = 800$ and 1600 panels are the Jenkins SO(324) result scaled up to those overdensities. At $\log\sigma^{-1} > 0$, the residuals increase, while at lower masses the rescaled $f(\sigma)$ underestimates the numerical results by $5\%$–$10\%$. Both of these effects are due to subhalos becoming exposed when halos are identified using higher overdensity. If a high-mass halo contains a large subhalo, the rescaling procedure will overestimate the mass of that object at higher $\Delta$. At low masses, the rescaling procedure does not account for the revealed substructures. The change in mass from $\Delta = 200$ to 1600 is $\sim50\%$ at $10^{14}\,h^{-1}\,M_\odot$. If subhalos are distributed within parent halos in a similar fashion to the
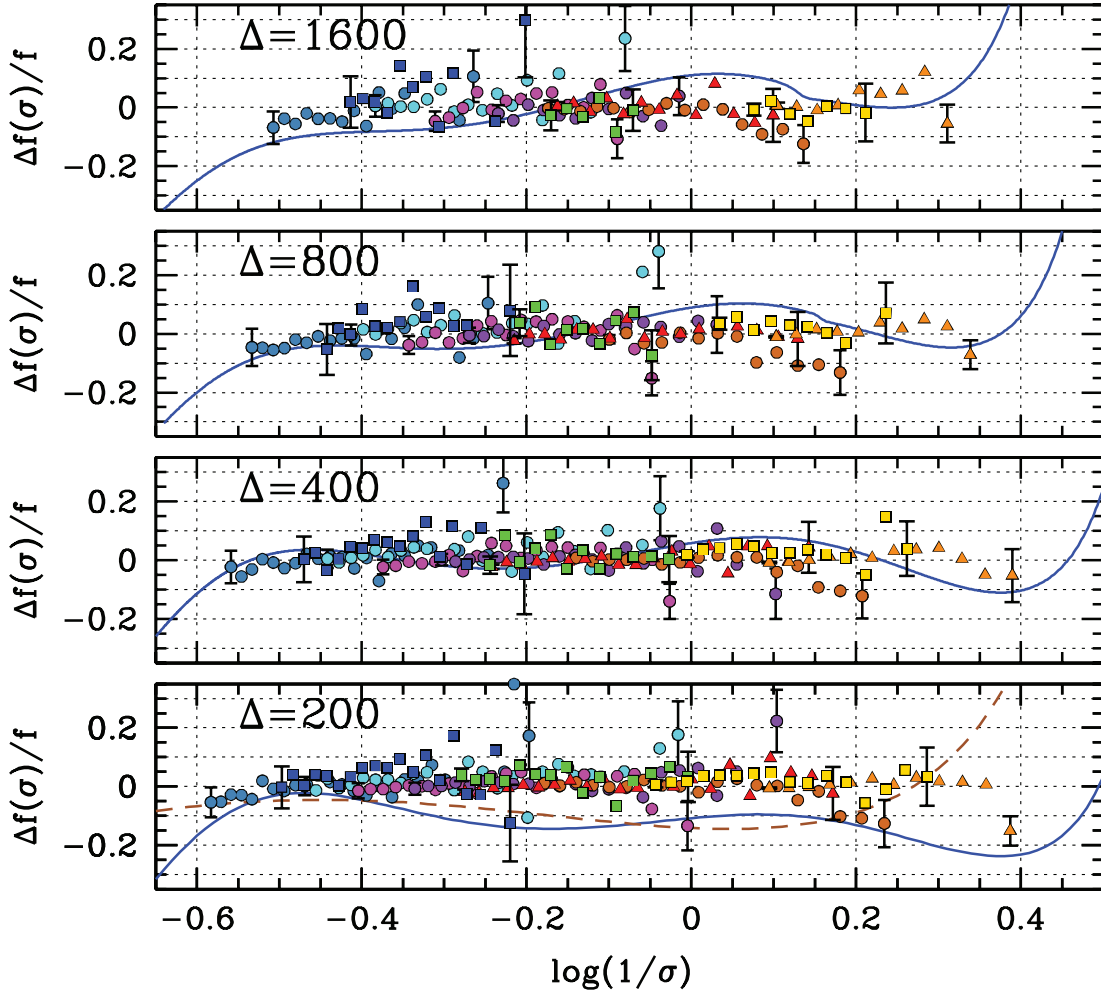
FIG. 7.—Residuals of the measured mass functions with respect to the best-fit analytic mass functions from Table 2 for all WMAP1 simulations at $z = 0$. Error bars are shown for the first and last point for each simulation, and only points with less than 10% error bars are plotted, with the exception of L80, for which 15% is the maximum. For $\Delta = 200$, the blue curve represents the Jenkins et al. (2001) SO180 mass function (scaling up to $\Delta = 200$ yields indistinguishable results). The red dashed curve represents the Sheth & Tormen (1999) mass function. For $\Delta = 400$, the blue curve represents the Jenkins et al. (2001) SO324 (scaled up to $\Delta = 400$). For $\Delta = 1600$ and $\Delta = 800$, the solid curve represents the Jenkins SO(324) mass function scaled up analytically assuming NFW profiles.

dark matter, then the rescaling procedure should underestimate the mass function by ~$0.5 \times 0.2 = 0.1$ (where 0.2 is the subhalo fraction for low-mass halos from Kravtsov et al. 2004).

Figure 8 shows that the best-fit parameters of $f(\sigma)$ vary with $\Delta$ smoothly. This means that interpolating between these best-fit parameters can be expected to yield accurate mass function parameters at any desired overdensity. In Appendix B we show examples of the interpolated mass functions, as well as fitting function for the $f(\sigma)$ parameters as a function of $\Delta$. The error bars are 1 $\sigma$ and are obtained by marginalizing over all other parameters. The errors on the amplitude $A$ are ~3%–4%, but this parameter is highly correlated with $b$ and the true scatter about the best-fit $f(\sigma)$ is $\lesssim 1\%$ at most masses.

The lower panel in Figure 8 shows the rms scatter in our constraints on $f(\sigma)$. The scatter was calculated by bootstrap resampling of the simulation set and repeating the fitting process on 100 bootstrap samples.[14] The shaded area is the variance of the

bootstrap fits. The light gray region represents results for $\Delta = 200$, while the dark gray region represents $\Delta = 1600$. Between $\log \sigma^{-1} = -0.2$ and 0.2 the scatter is less than 1% ($M = 10^{11.5}$ and $10^{15}$ $h^{-1}$ $M_\odot$ for the WMAP1 cosmology). Outside this mass range the results diverge due to lack of coverage by the simulations. Because the WMAP1 simulations dominate by number, these constraints should be formally regarded as the accuracy of the fit for the WMAP1 cosmology.

Figure 9 compares the calibrated mass functions from Table 2 with the measured mass functions from the WMAP3 simulations (i.e., the last seven entries in Table 1). Column (9) of Table 2 contains values of $\chi^2/\nu$ for the WMAP3 simulations only. The $\chi^2/\nu$ are somewhat larger than for the WMAP1 runs at all overdensities, even though the WMAP3 residuals do not seem to be systematically offset from the global $f(\sigma)$ fits. We test this statistically by refitting for the parameters of equation (3) using *only* the WMAP3 simulations. The $\chi^2/\nu$ values are listed in column (10) of Table 2. For each $\Delta$, the $\chi^2$ of the fit is only reduced marginally. In the mass range covered by our simulations, the difference between the global $f(\sigma)$ functions and those derived from the WMAP3 simulations differ by $\lesssim 2\%$, but with a ~4% uncertainty in the normalization of the WMAP3-only fitting function, derived from the bootstrap method described above. Thus, we conclude that the

---

[14] Because the 50 realizations of L1280 outnumber all the rest of the simulations (which only number 17), we create bootstrap samples by first sampling from the list of L1280 realizations, then sampling from the rest of the simulation set. This guarantees a fair sampling of the range of $\sigma^{-1}$ probed by the simulations. If we do not do this, many bootstrap samples will only contain mass function with results above $M \gtrsim 2 \times 10^{14}$ $h^{-1}$ $M_\odot$, which would artificially inflate the size of the low-mass errors.
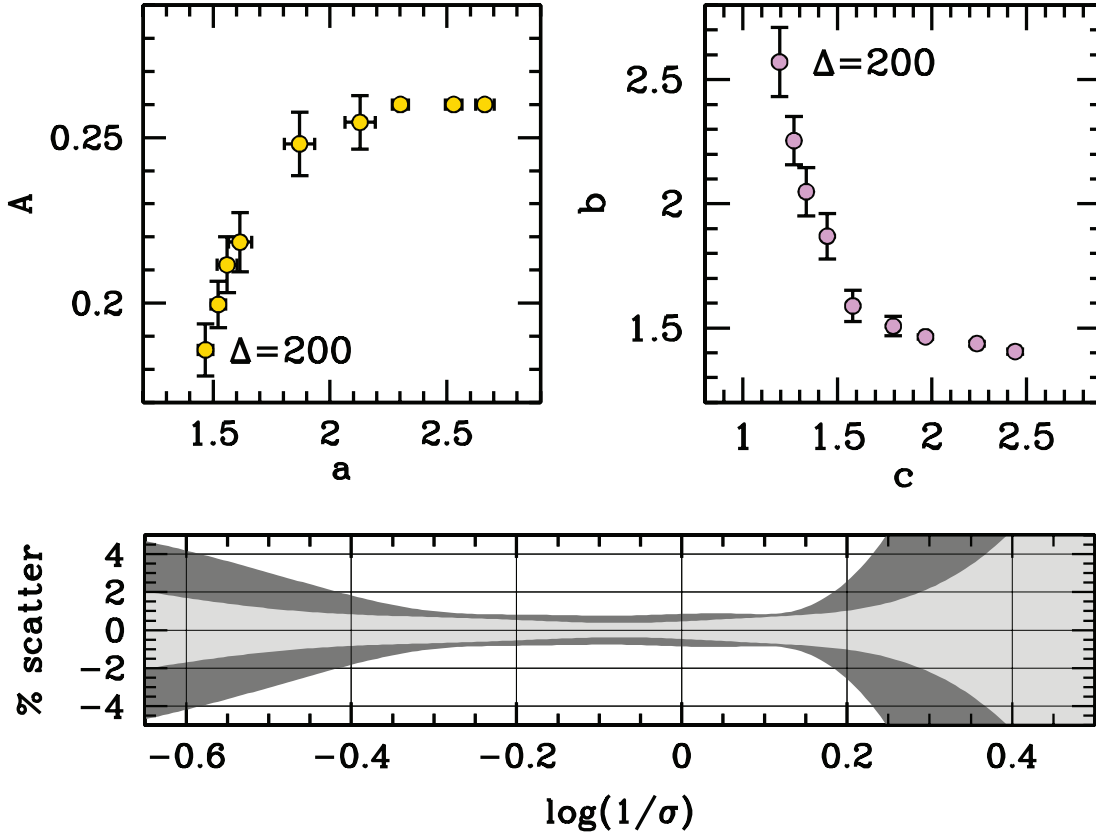
Fig. 8.—Trajectories of the best-fit parameters of $f(\sigma)$ from Table 2. In each panel, the order of the points is from low-$\Delta$ to high-$\Delta$ (*left to right*). Error bars represent 1 $\sigma$ variance of parameters from the MCMC chain. (*a*) Normalization $A$ vs. power-law slope $a$. (*b*) Power-law amplitude $b$ vs. the cutoff scale $c$. The lower panel shows the rms scatter of mass functions from 100 bootstrap samples, creating by sampling the simulation list. The light gray region is for $\Delta = 200$, while the dark gray region is for $\Delta = 1600$.

higher $\chi^2$ values are not due to a systematic change in $f(\sigma)$ due to variations in cosmology, but rather scatter in the simulations themselves at the $\sim$5% level, excluding obvious outliers where Poisson noise dominates.

### 3.3. Redshift Evolution

Figure 10 shows the evolution of the $\Delta = 200$ mass function for four different redshifts from $z = 0$ to 2.5. Results are plotted for the subset of simulations for which we have previous redshift outputs. When modeled as pure amplitude evolution, the mass function evolves as $(1 + z)^{-0.26}$. However, it is also clear that the shape of $f(\sigma)$ is evolving with redshift such that the amplitude at $\log \sigma^{-1} > 0$ decreases at a higher rate. This is more evident in Figure 11, in which $f(\sigma)$ at $\Delta = 1600$ is shown for the same redshifts. As $\Delta$ increases, both the evolution in the amplitude and shape of $f(\sigma)$ become stronger.

In Figures 10 and 11, the solid curves show a model in which the first three parameters of $f(\sigma)$ are allowed to vary as a power law of $1 + z$;

$$A(z) = A_0(1 + z)^{-0.14}, \quad (5)$$

$$a(z) = a_0(1 + z)^{-0.06}, \quad (6)$$

$$b(z) = b_0(1 + z)^{-\alpha}, \quad (7)$$

$$\log \alpha(\Delta) = -\left[\frac{0.75}{\log(\Delta/75)}\right]^{1.2}, \quad (8)$$

where the zero subscript indicates the value obtained at $z = 0$ in Table 2. Modulation of $A$ controls the overall amplitude of $f(\sigma)$,

while $a$ controls the tilt, and $b$ sets the mass scale at which the power law in $f(\sigma)$ becomes significant. Modifying $b$ results in a shift between the amplitudes at low and high $\log \sigma^{-1}$; thus, it encapsulates the changes in $f(\sigma)$ with $\Delta$ seen in Figures 10 and 11. Although the redshift scaling introduced here matches the results at $z \leq 2.5$ accurately, residuals of $\gtrsim$5% emerge at $z = 2.5$. It is possible that the evolution between $z = 1.25$ and 2.5 is slowing down. Because the numerical results at $z = 2.5$ are quite noisy and cover only a small range in $\sigma^{-1}$, our results at this value of $z$ and extrapolation to higher redshifts must be checked with other simulations. Extrapolating equation (5)–(8) to $z = 10$ produces an $f(\sigma)$ that is reduced by $\sim$50% with respect to $z = 0$. This seems unlikely given current studies but needs to be checked with a consistent halo finding algorithm.

Reed et al. (2007) parameterize the redshift-dependent mass function in terms of both $\sigma$ and the effective spectral index of the linear power spectrum, $n_{\rm eff}$. These authors use this parameterization to model the mass function at $z > 10$, where differences in the slope of $n_{\rm eff}$ from $z = 0$ are large. This approach is ill suited for modeling the evolution at $z < 3$, where there is very little change in the effective spectral index. This implies that the parameter dominating the redshift evolution (at these redshifts) is $\Omega_m$ rather than the shape of the power spectrum.

It is interesting to note that the evolution in the exponential cutoff scale is minimal. Any evolution in this mass scale would yield quantitatively different residuals than those seen in Figure 10 and 11. Namely, the residuals would show pronounced curvature at $\log \sigma^{-1} > 0$. Our results show that the dominant effect is a shift in the normalization in the mass function rather than the cutoff mass scale. Thus, our results are not consistent with $f(\sigma)$ being
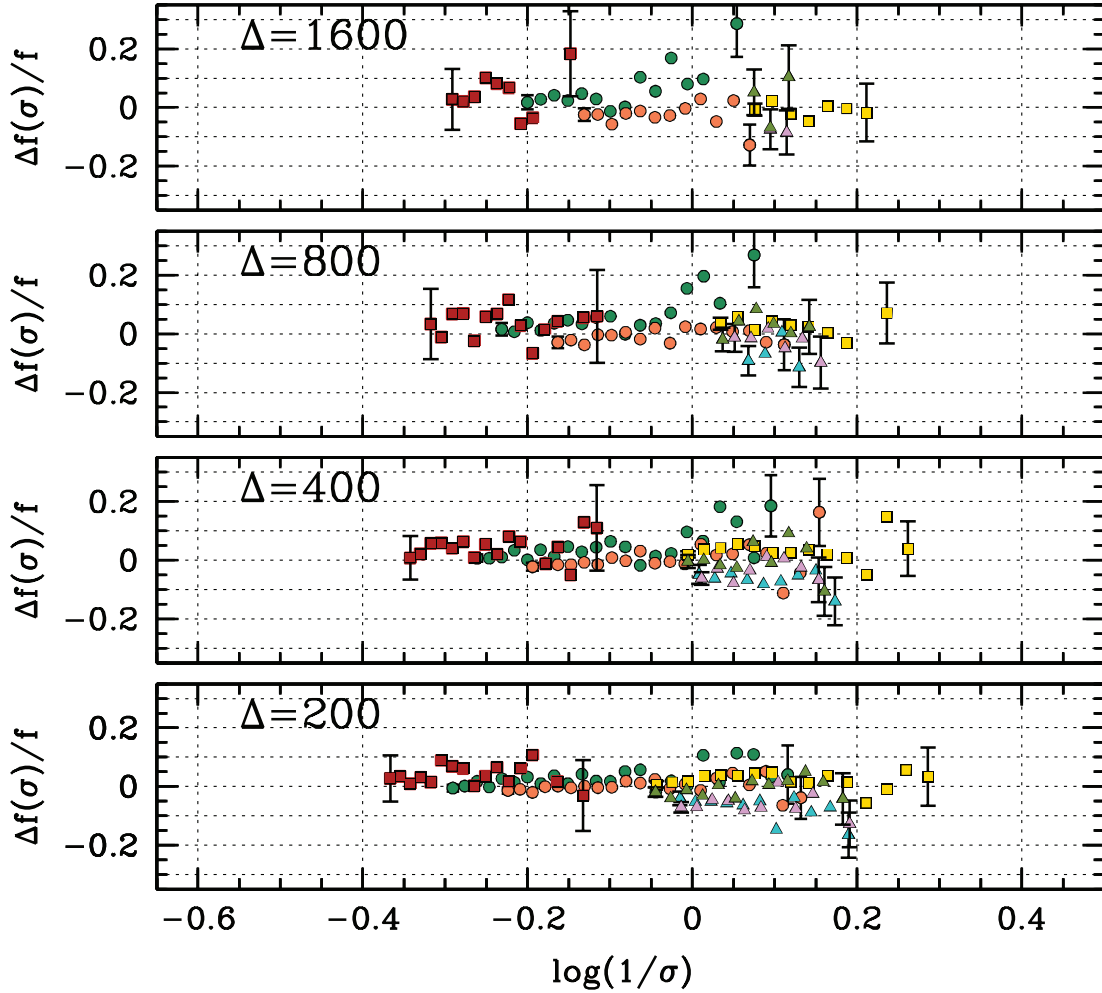
Fig. 9.—Residuals of the measured mass functions with respect to the best-fit analytic mass function from Table 2 for all WMAP3 simulations at $z = 0$. Error bars are shown for the first and last point for each simulation, and only points with less than 10% error bars are plotted, with the exception of L80W, for which 15% is the maximum.

universal as a function of *virial* overdensity because $\Delta_{\rm vir}$ evolves with redshift. Nor are our results consistent with the mass function being universal at a fixed overdensity with respect to the critical density (rather than defining $\Delta$ with respect to the background, as we do here).

The Jenkins et al. (2001) study reports no detected evolution of the FOF or SO mass functions with redshift. More recent results quantify the evolution of the FOF at high redshift, $z \gtrsim 10$, to be 5%–10% (Lukic et al. 2007; Reed et al. 2007; Cohn & White 2008). However, friends-of-friends identified halos may have a different response to changes in the redshift evolution of halo profiles. Merging rates vary with redshift, and this may be reflected in the FOF tendency to bridge distinct structures. Figure 12 shows the redshift evolution for friends-of-friends selected halos in the L500 and L250 boxes. The panels in the left column show the results for halos identified with a linking length of 0.2. Residuals are calculated with respect to the Warren et al. (2006) fitting formula with their best-fit parameters, plotted down to halos containing 100 particles. The friends-of-friends masses have not been corrected for any systematic errors (eq. [2] in Warren et al. 2006), resulting in the slight negative slope to the residuals at low masses. The mass function shows some redshift evolution, but only of order $\sim$10% at $z = 1.25$, or roughly half that in Figure 10.

The right column shows the results for halos identified with a linking length of $l = 0.1$. The smaller linking length identifies

halos with higher overdensities. The residuals are with respect to $f(\sigma)$ for $\Delta = 1600$. For this linking length, the redshift evolution is stronger than for $l = 0.2$, and the shape of the FOF mass function changes dramatically. As a whole, these results indicate that the mass function is also nonuniversal for FOF halos, with the degree of nonuniversality depending on the linking length used.

These results are in general agreement with those of other recent studies that considered evolution of the mass function for FOF halos, although the overall picture of how the mass function evolves with redshift is not yet clear. The simulation results of Lukic et al. (2007) exhibited $\sim$−5% residuals with respect to the $z = 0$ Warren et al. mass function as $z = 5$, but with a monotonic trend of rising residuals with increasing redshift. The FOF mass function in the Millennium Simulation shows roughly 20% evolution from $z = 0$ to 10 (Reed et al. 2007). Finally, Fakhouri & Ma (2008) recently showed that the Millennium Simulation FOF mass function, once corrected for spurious FOF linking between halos, evolves by $\sim$20% from $z = 0$ to 1. This is consistent with our findings, but note that the volume of the Millennium Simulation and statistics at large masses is substantially worse than in our set of simulations.

## 4. SUMMARY AND DISCUSSION

We have presented a new fitting function for halo abundances and their evolution in the $\Lambda$CDM cosmology. The fitting function
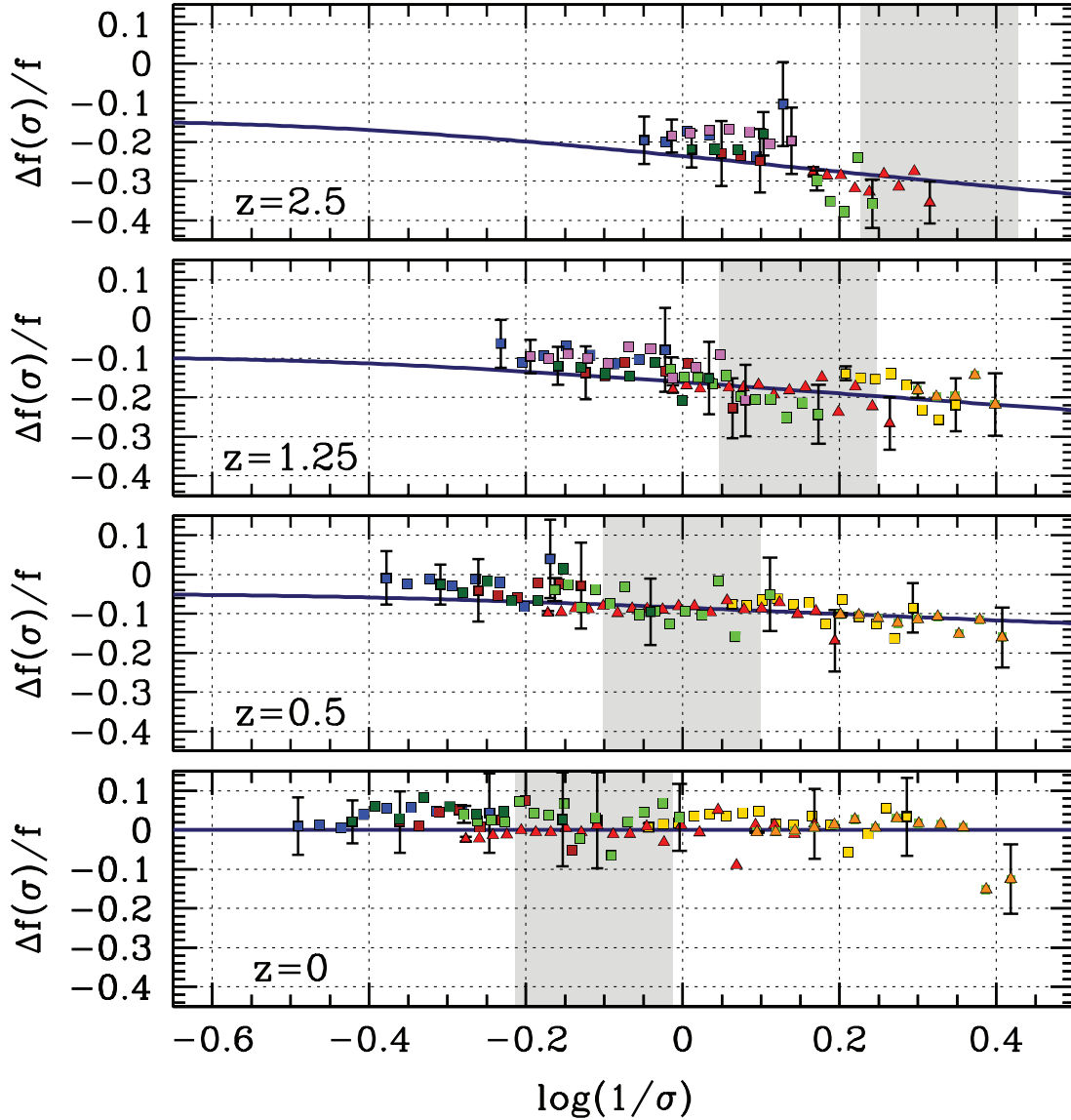
Fig. 10.—Redshift evolution of the $\Delta = 200$ mass function. Each panel shows the residuals of the $z = 0$ mass function with respect to the measured mass functions at $z = 0, 0.5, 1.25$, and $2.5$. Note that the simulation set used here is a combination of WMAP1 and WMAP3 boxes. Error bars are shown for the first and last points for each simulation, and only points with $<10\%$ are shown, with the exception of the L80 and L80W, for each 15% is the limit. The shaded region brackets $10^{13}$ to $10^{14}\, h^{-1}\, M_\odot$. The solid curves represent the $z = 0$ mass function modified by eqs. (5)–(8).

can be used to predict halo mass functions for spherical aperture masses defined with an arbitrary overdensity over a wide range of values. For the WMAP1 cosmology our results are accurate at the percent level in the mass range relevant for cluster cosmology. For the WMAP3 cosmology our results are accurate to $\lesssim 5\%$. One of our main results is that the mass function is nonuniversal, and varies in a systematic way with redshift in the interval $z = [0, 2.5]$, with the abundance of halos at a given $\log \sigma^{-1}$ monotonically decreasing with increasing $z$.

We have parameterized redshift evolution of $f(\sigma)$ as a simple scaling of the $z = 0$ fitting parameters with $(1 + z)^\alpha$. We note that if this evolution is driven by changes in $\Omega_m$ with $z$, it may be more robust to model $f(\sigma, z)$ as a function of the growth rate rather than $1 + z$. Our simulation set does not probe a large enough cosmological parameter space to detect differences due to different growth factors. However, this will become important when investigating how the mass function evolves in dark energy cosmologies, in

which the primary change in structure formation is a different growth function of perturbations.

Our finding of evolving, nonuniversal $f(\sigma)$ is quantitatively different from the results of previous analyses that use the friend-of-friends method for halo identification, which generally show weaker evolution and greater degree of universality of the function $f(\sigma)$. We argue that the likely explanation for this difference is greater sensitivity of the SO defined mass to the redshift evolution of halo concentrations. As discussed previously, SO masses are the integrated halo profiles within a specified radius and lower halo concentrations result in lower masses at fixed abundance (or, conversely, fewer halos at fixed mass). The fact that the high-mass end of the mass function (where concentrations at $z = 0$ are lower and the mass within $R_{200}/c_{200}$ is a significant fraction of the total mass) evolves somewhat faster than the low-mass end argues that evolution of concentrations plays a significant role in the evolution of $f(\sigma)$.
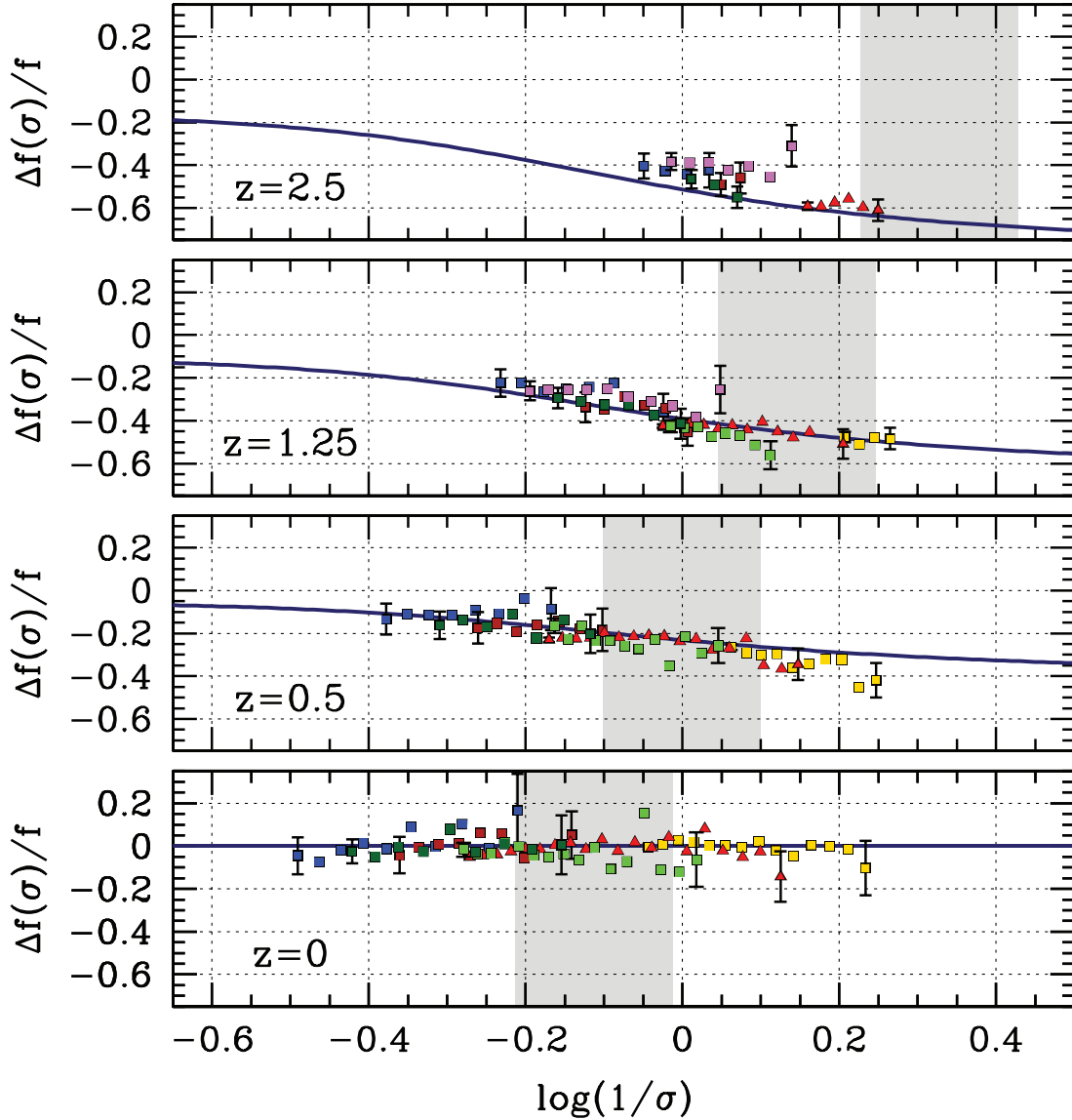
Fig. 11.—Redshift evolution of the $\Delta = 1600$ mass function. Each panel shows the residuals of the $z = 0$ mass function with respect to the measured mass functions at $z = 0, 0.5, 1.25,$ and $2.5$. Note that the simulation set used here is a combination of WMAP1 and WMAP3 boxes. Results are plotted down to halos with 400 particles, as opposed to the limit of 1600 used in fitting $f(\sigma)$. All points with errors $<15\%$ are plotted. The shaded region brackets $10^{13}$ to $10^{14}$ $h^{-1}$ $M_\odot$. The solid curves represent the $z = 0$ mass function modified by eqs. (5)–(8).

The evolution of halo concentrations is mostly driven by the change in $\Omega_m$ with redshift. This implies that $f(\sigma)$ in cosmologies with substantially different matter densities at $z = 0$ will be systematically different from the one we find here (perhaps closer to our $z > 1$ results). There are indications that this is indeed the case. The H384$\Omega$ simulation, with $\Omega_m = 0.2$, is above $f(\sigma)$ by $\sim5\%$ at $z = 0$. The Jenkins et al. (2001) fitting function for $\Delta = 180$ was calibrated on simulations with $\Omega_m = 1$, producing a fit $\sim15\%$ below our results at the same overdensity. The Jenkins SO(180) mass function is close to our $\Delta = 200$ results at $z = 1.25$, where $\Omega_m$ is approaching unity.

The lower evolution of the FOF mass function with redshift can be understood from Figure 2. The distribution of mass ratios between FOF and SO halos changes between $z = 0$ and $1.25$. The median mass ratio, $M_{\rm SO}/M_{\rm FOF}$, decreases while the scatter increases at higher $z$ due to more linking of *distinct* objects. The number of distinct objects at a fixed $\log \sigma^{-1}$ decreases, but the

higher incidence of linking offsets this effect. Thus, the weaker evolution of the FOF mass function is due to this linking of separate collapsed halos and is largely artificial. The better universality of $f(\sigma)$ may still seem like an advantage of the FOF mass function. However, as we discussed in this paper, the large and redshift-dependent scatter between SO and FOF masses implies similarly large and redshift-dependent scatter between FOF masses and cluster observables. This makes robust interpretation of observed cluster counts in terms of the FOF halo counts problematic.

Our fitting function is calibrated over the range $-0.6 \lesssim \log \sigma^{-1} \lesssim 0.4$, which at $z = 0$ spans a range of halo masses roughly $10^{10.5}$ $h^{-1}$ $M_\odot \lesssim M \lesssim 10^{15.5}$ $h^{-1}$ $M_\odot$, depending on the specific choice of cosmology. In Figure 13 we show how this mass range evolves with redshift. By $z = 3$, the lower mass limit is $\sim10^5$ $h^{-1}$ $M_\odot$. At this redshift, our fitting function is in agreement with the numerical results of Colín et al. (2004), which probe
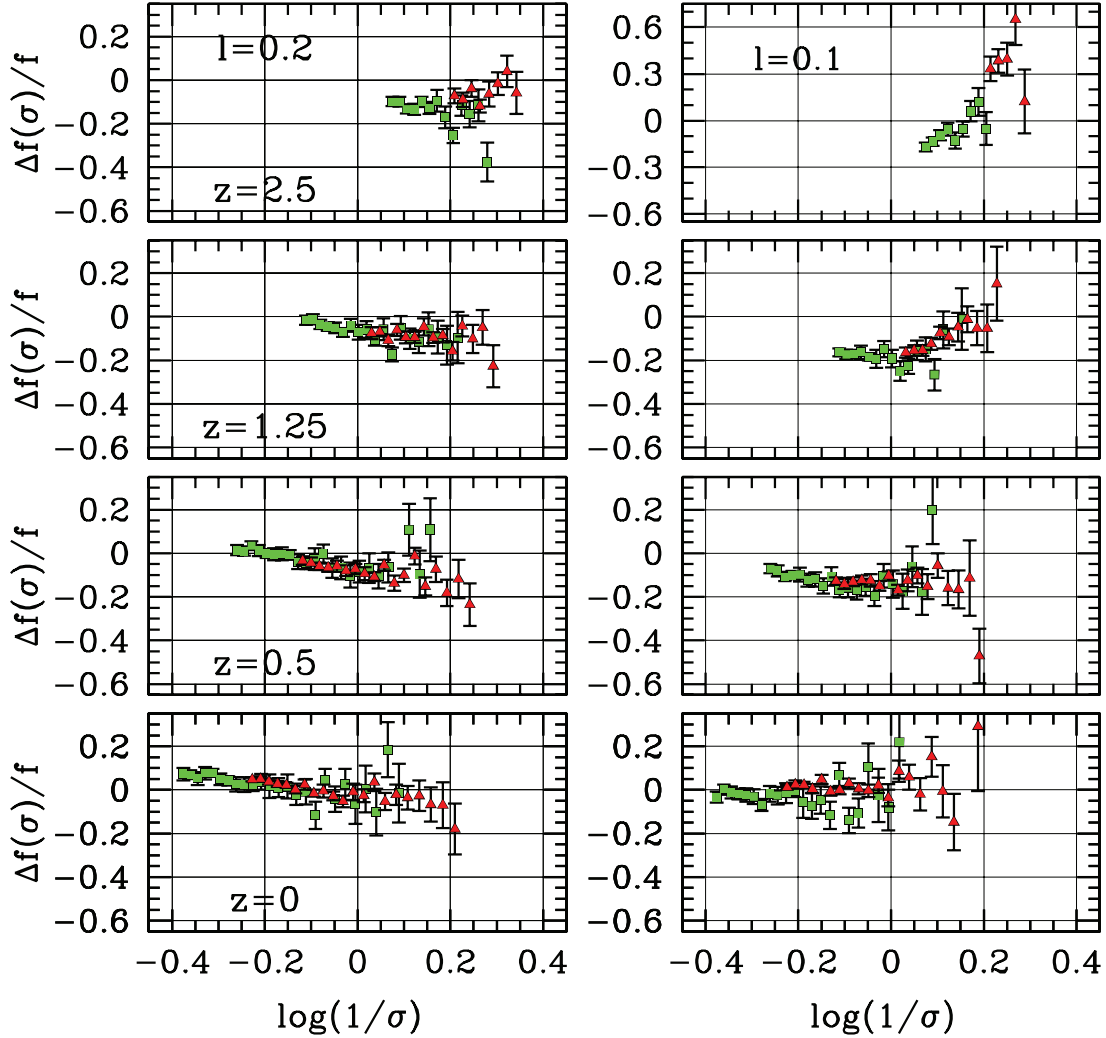
Fɪɢ. 12.—Evolution of the FOF mass function for linking lengths of $l = 0.2$ (*left*) and $l = 0.1$ (*right*). The simulations used are L500 and L250. The L500 simulation has been downsampled to 1/8 the original particle number. For $l = 0.2$, the residuals are plotted with respect to the Warren et al. (2006) function. Mass functions are plotted down to 100 particles per halo but have not been corrected for discreteness effects (i.e., eq. [2] in Warren et al.). For $l = 0.1$, the residuals are plotted with respect to the $\Delta = 1600$ mass function from Table 1. Note the larger range of the $y$-axis at $z = 2.5$ for $l = 0.1$. The FOF mass function evolves less than the SO mass function, but this largely a numerical effect due to increased linking of distinct halos.

the mass range $10^5 \, h^{-1} \, M_\odot \leq M \leq 10^9 \, h^{-1} \, M_\odot$. At higher redshifts, $\log \sigma^{-1}$ is a slowly varying function of mass, making the lower mass limit evolve rapidly. Because our calibration of the redshift dependence of the mass function parameters extends only to $z = 2.5$, we caution against extrapolation of equations (5)–(8) to significantly higher redshifts. As noted above, $f(\sigma)$ is evolving less rapidly from $1.25 < z < 2.5$ than from $0 < z < 1.25$. Thus using the $z = 2.5 f(\sigma)$ should yield a mass function with reasonable accuracy at higher $z$, but must be verified with additional simulations.

The range of cosmologies probed here is narrow given the volume of parameter space, but it is wider than the allowed range given recent results from CMB in combination with other large-scale measures (Komatsu et al. 2008). For general use that does not require 5% accuracy, extending our results somewhat outside this range will produce reasonable results. It is unlikely that variations in the shape and amplitude of the power spectrum will yield significantly different forms of $f(\sigma)$. As discussed above, however, large variations in $\Omega_m$ at $z = 0$ (i.e., $\Omega_m = 0.1$ or 1), are not likely to be fit by our $z = 0$ mass function within our 5% accuracy. Models with a higher matter density at $z = 0$ can be ap-

proximated by using our calibrated $f(\sigma)$ at the redshift for which $\Omega_m(z)$ is equal to the chosen value.

The next step in the theoretical calibration of the mass function for precision cosmology should include careful examination of subtle dependencies of mass function on cosmological parameters (especially on the dark energy equation of state), effects of neutrinos with nonzero mass, effects of non-Gaussianity (Grossi et al. 2007; Dalal et al. 2008), etc. Last, but not least, we need to understand the effects of baryonic physics on the mass distribution of halos and related effects on the mass function, which can be quite significant (Rudd et al. 2008). The results of Zentner et al. (2007) indicate that the main baryonic effects can be encapsulated in a simple change of halo concentrations, which would result in a uniform shift of $M_\Delta$ and a uniform correction to $f(\sigma)$. Whether this is correct at the accuracy level required remains to be demonstrated with numerical simulations.

Our study illustrates just how daunting is the task of calibrating the mass function to the accuracy of $\lesssim 5\%$. Large numbers of large-volume simulations are required to estimate the abundance of cluster-sized objects, but a high dynamic range is required to properly resolve their internal mass distribution and subhalos. The
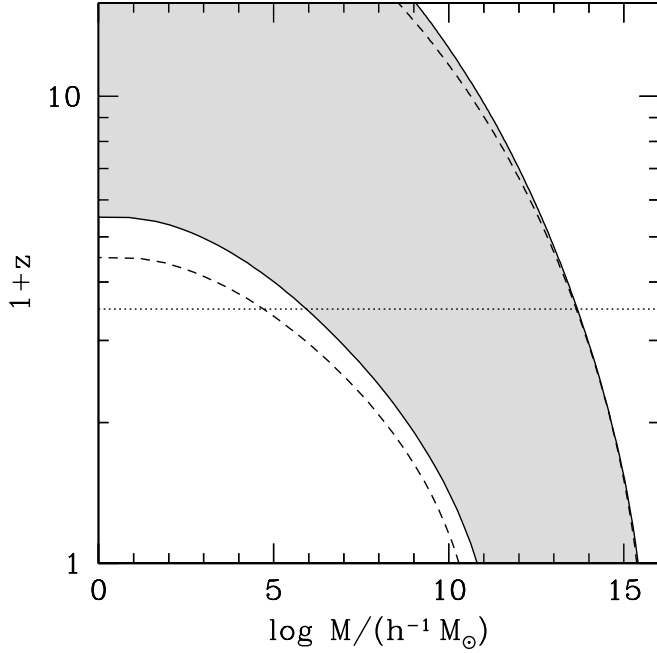
Fig. 13.—Halo mass range corresponding to the range of $\log \sigma^{-1}$ on which $f(\sigma)$ is calibrated. The shaded region bounded by the solid curves shows how this mass range evolves with redshift for the WMAP1 cosmology. The dashed curves show the upper and lower mass limits for the WMAP3 cosmology of the L80W simulation. The dotted line indicates the maximum redshift output of our simulation set.

numerical and resolution effects should be carefully controlled, which requires stringent convergence tests. In addition, the abundance of halos on the exponential cutoff of the mass function can be influenced by the choice of method to generate initial conditions and the starting redshift, as was recently demonstrated

by (see also Appendix A) Crocce et al. (2006). All this makes exhaustive studies of different effects and cosmological parameters using brute force calibration of the kind presented in this paper for the ΛCDM cosmology extremely demanding. Clever new ways need to be developed both in the choice of the parameter space to be investigated (Habib et al. 2007) and in complementary studies of various effects using smaller, targeted simulations.

## APPENDIX A

## TESTS OF THE INITIAL CONDITIONS

In a recent study, Crocce et al. (2006) investigated differences between using the standard first-order Zel'dovich approximation (ZA) and second-order Lagrangian perturbation theory (2LPT) for generating initial conditions of cosmological simulations. ZA assumes that particle trajectories are straight lines, but for large density fluctuations trajectories should curve due to tidal effects. Thus, if a simulation is initialized at the epoch where the overdensity is large in some regions, the resulting error in particle trajectories will lead to "transients" in the evolution of perturbations (see also Scoccimarro 1998), which can persist to $z = 0$. This effect is strongest for the regions containing rarest peaks of largest height that tend to evolve into the largest galaxy clusters at low redshift. In their simulation results, Crocce et al. find a $\sim 10\%$ discrepancy at $M \sim 10^{15} \, h^{-1} \, M_\odot$ in $z = 0$ mass functions between 2LPT and ZA with starting redshift of $z_i = 24$. This discrepancy is expected to grow more significant at higher redshift at fixed halo mass. The effect is particularly worrisome for precision calibration of abundance of the most massive objects at any redshift (those objects that are currently collapsing or have only recently collapsed). In this Appendix we present tests of the effects of the initial redshift on the mass function and explain why we have discarded some of the large-volume simulations from our analysis.

The top panel in Figure 14 shows a graphical key of the three large-box HOT simulations used in the Warren et al. (2006) fit that we do not utilize in our mass function fits. These simulations have starting redshifts of $z_i = 34$, 28, and 24 (with $z_i$ decreasing with increasing box size). In addition, we also have results from the Hubble volume (HV) simulation, a 3000 $h^{-1}$ Mpc simulation (Evrard et al. 2002). We use the same SO halo catalog presented in Evrard et al. (2002) which used a density criterion of 200 times the critical density rather than the mean. Thus we have scaled the halo masses from $\Delta = 666$ to 200, assuming NFW profiles as detailed in § 2. Lastly, we have included a resimulation of the L1000W ART box which has been initialized at $z_i = 35$ rather than $z_i = 60$ using the same set of random phases and ZA at both starting redshifts.

The bottom panels of Figure 14 show the residuals of the simulation mass function from the best fit to our core simulation set at $z = 0$ and 1.25. At $10^{14} \, h^{-1} \, M_\odot$, all simulations are in excellent agreement. However, at $10^{15} \, h^{-1} \, M_\odot$, the HOT boxes are $\sim 10\%$–20% below the $f(\sigma)$ obtained from the 2LPT simulations and ART L1000W run. The mass function of the HV simulation, with $z_i = 35$, is also $\sim 15\%$ below the 2LPT simulations.

At $z = 0$, there is a $\sim 2\%$ difference between low-$z_i$ ART box and the higher $z_i$ version used in the fitting. This is smaller than the difference between mass functions for the Crocce et al. (2006) simulations with $z_i = 24$ and 49, which may be due to sample variance. However, the difference between the two ART boxes increases at higher redshift. The ART box with $z_i = 60$ is in good agreement with
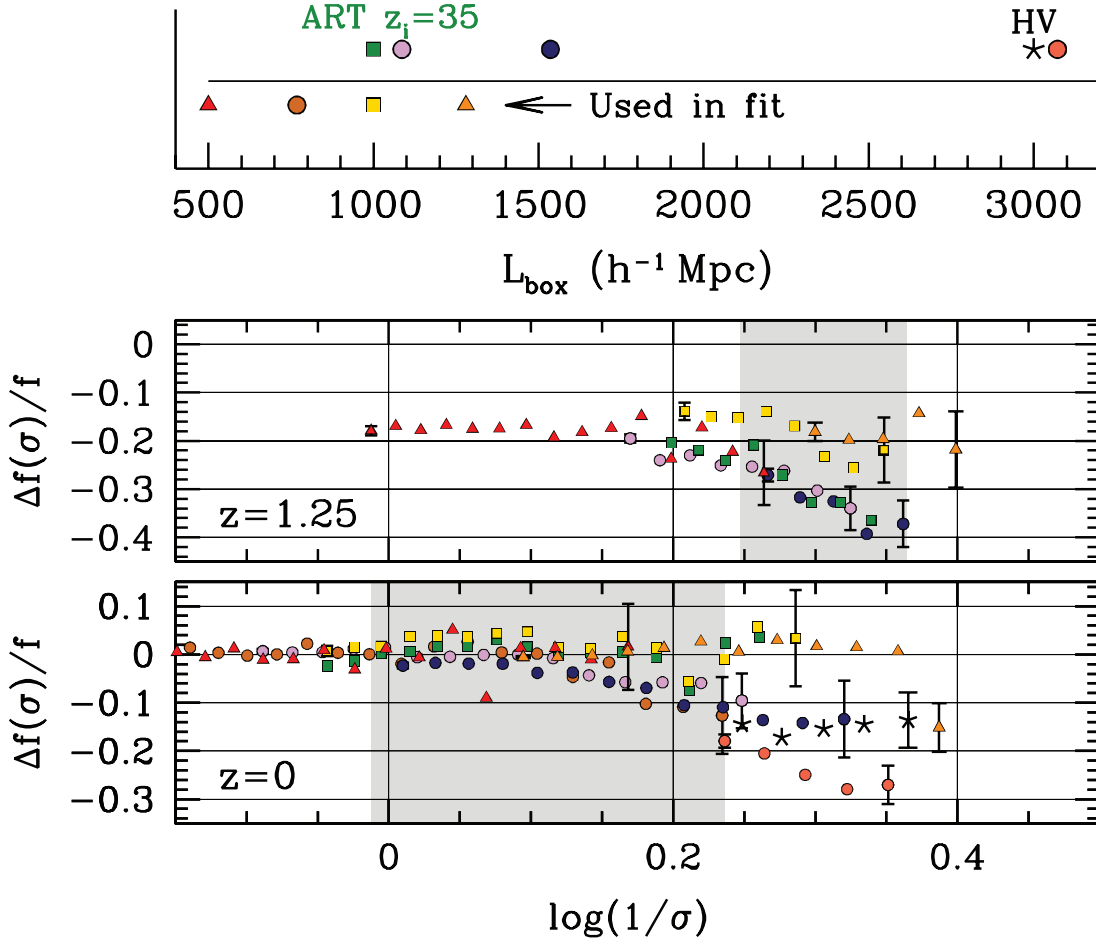
FIG. 14.—Comparison between the large-box simulations used in the text and those in Warren et al. (2006) and Evrard et al. (2002). *Top*: Box sizes and point types for the three HOT boxes and the Hubble Volume are shown above the horizontal line. In addition, a version of the L1000W ART box, started at lower redshift, is also included in the comparison. The large-box simulations used from Table 1 are also included below the horizontal line. *Bottom*: comparison of the $\Delta = 200$ mass functions to the best-fit $f(\sigma)$ at $z = 0$. *Middle*: Results at $z = 1.25$. In the $z = 0$ panel, the shaded region indicates $10^{14}\ h^{-1}\ M_\odot < M < 10^{15}\ h^{-1}\ M_\odot$ in the WMAP1 cosmology. In the $z = 1.25$ panel, the shaded region indicates $10^{14}\ h^{-1}\ M_\odot < M < 10^{14.5}\ h^{-1}\ M_\odot$.

the 2LPT simulations at $z = 1.25$, implying that convergence has been reached at a lower $z_i$ than shown in Crocce et al. The run with $z_i = 35$, however, is 20%–40% lower than the best fit at large masses.

It is not yet entirely clear whether the source of the discrepancies in the mass functions at the highest masses can be attributed solely to the errors of the ZA-generated initial conditions. The difference between the large-volume HOT boxes and the 2LPT results are larger than expected from just the ZA errors. Also, both ART boxes, with $z_i = 35$ and 60, are in agreement with the 2LPT simulations at $z = 0$. Other factors, such as resolution effects on the halo density profiles, may play a dominant role in the discrepancy exhibited by both the HOT boxes and the HV simulation. Regardless of the source of the discrepancy, it is clear that the large-volume HOT boxes and HV simulations are systematically different from other higher resolution simulations. We therefore do not include them in our analyses.

In summary, the simulations which we use to derive our constraints on the high-mass end of the halo mass function are all robust against changing initial redshift. The 2LPT simulations have been thoroughly tested in Crocce et al. (2006). The L1000W and L500 simulations, utilizing ZA with $z_i \gtrsim 50$, show consistent results with the 2LPT simulations at multiple redshifts. However, quantifying the effects of initial conditions, finite simulation volume, and possible numerical artifacts at the $\lesssim 1\%$ level will require significant additional work.

## APPENDIX B

## INTERPOLATION OF MASS FUNCTION PARAMETERS

To facilitate the use of our results in analytic calculations, we provide fitting functions for the parameters of $f(\sigma)$ as a function of $\log \Delta$. The dependence of each parameter in the mass function is reasonably well described by

$$A = \begin{cases} 0.1(\log \Delta) - 0.05 & \text{if } \Delta < 1600, \\ 0.26 & \text{if } \Delta \geq 1600, \end{cases} \tag{B1}$$

$$a = 1.43 + (\log \Delta - 2.3)^{1.5}, \tag{B2}$$

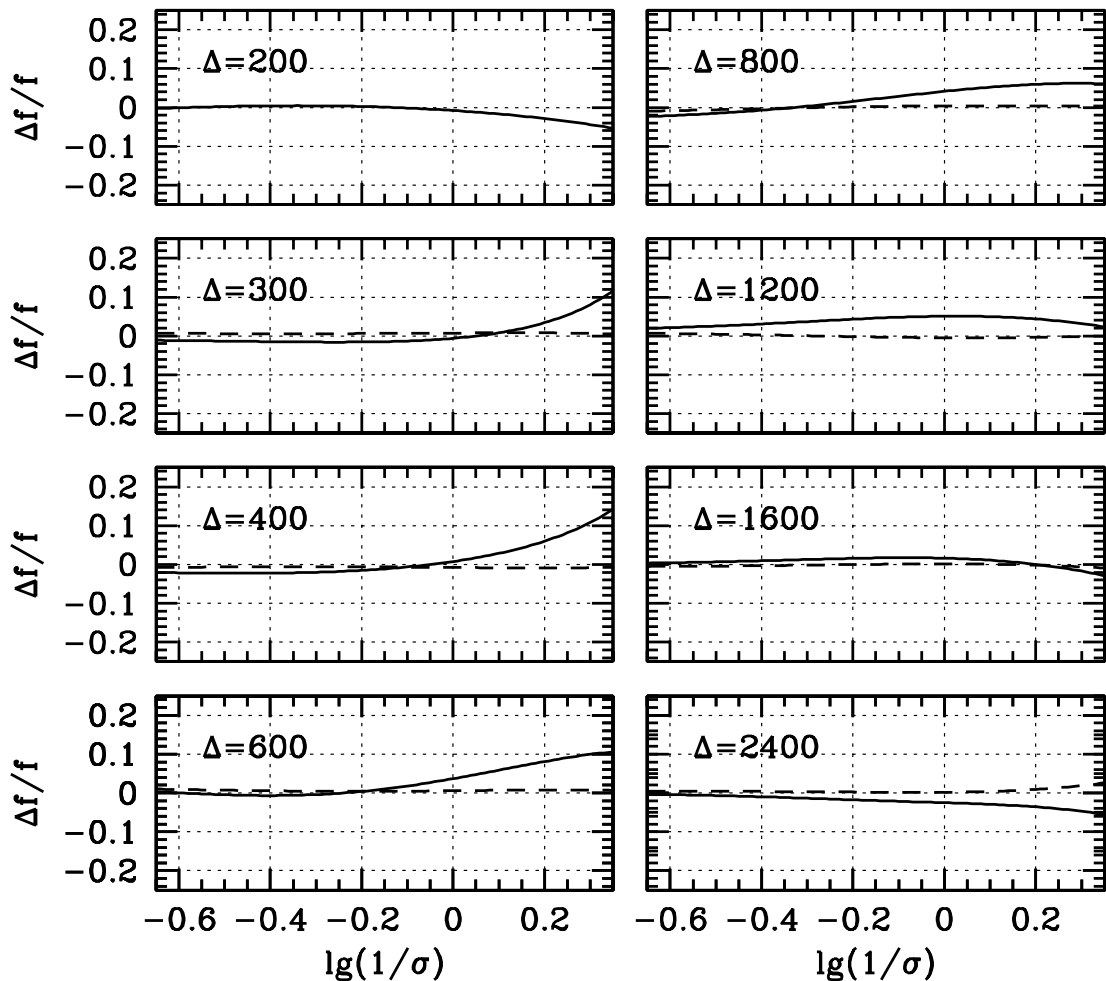$$b = 1.0 + (\log \Delta - 1.6)^{-1.5}, \tag{B3}$$

Fig. 15.—Accuracy of the fitting functions presented in Appendix B for calculating the parameters of $f(\sigma)$ as a function of $\Delta$ (*solid lines*). All curves are residuals with respect to the best-fit results of $f(\sigma)$ from Table 2. For all overdensities except $\Delta = 600$, the accuracy of $f(\sigma)$ is $\lesssim 5\%$. The dashed lines show the accuracy of $f(\sigma)$ when using spline interpolation, which is accurate to $\lesssim 2\%$ for all $\Delta$ and $\log \sigma^{-1}$.

$$c = 1.2 + (\log \Delta - 2.35)^{1.6}. \tag{B4}$$

All logarithms are base 10. Because the parameters of $f(\sigma)$ are not completely smooth with $\log \Delta$, these functions yield mass functions that are accurate to only $\lesssim 5\%$ for most values of $\Delta$, but can degrade to $\lesssim 10\%$ at $\log \sigma^{-1} > -0.7$ for some overdensities. Figure 15 demonstrates the accuracy of the fitting functions with respect to the results from Table 2. For higher accuracy, we recommend spline interpolation of the parameters as a function of $\log \Delta$. Figure 15 shows the results of the spline interpolation when obtaining the parameters of $f(\sigma)$. We provide the second derivatives of the $f(\sigma)$ parameters for calculation of the spline coefficients (e.g., § 3.3 in Press et al. 1992) in Table 3.

## APPENDIX C

## AN ALTERNATE, NORMALIZED FITTING FUNCTION

The fitting function given in equation (3) is an excellent descriptor of the data over the range of our data, but at $\log \sigma^{-1} \lesssim -1.0$, $f(\sigma)$ asymptotes to a constant value. For some applications, specifically halo model calculations of dark matter clustering statistics, it is necessary

### TABLE 3
### Second Derivatives of $f(\sigma)$ Parameters

| $\Delta$ | $A$ | $a$ | $b$ | $c$ |
|---|---|---|---|---|
| 200...................... | 0.00 | 0.00 | 0.00 | 0.00 |
| 300...................... | 0.50 | 1.19 | −1.08 | 0.94 |
| 400...................... | −1.56 | −6.34 | 12.61 | −0.43 |
| 600...................... | 3.05 | 21.36 | −20.96 | 4.61 |
| 800...................... | −2.95 | −10.95 | 24.08 | 0.01 |
| 1200...................... | 1.07 | 2.59 | −6.64 | 1.21 |
| 1600...................... | −0.71 | −0.85 | 3.84 | 1.43 |
| 2400...................... | 0.21 | −2.07 | −2.09 | 0.33 |
| 3200...................... | 0.00 | 0.00 | 0.00 | 0.00 |

TABLE 4
Normalized Mass Function Parameters for $g(\sigma)$ at $z = 0$

| $\Delta$ | $B$ | $d$ | $e$ | $f$ | $g$ | $\chi^2/\nu$ |
|---|---|---|---|---|---|---|
| 200...... | 0.482 | 1.97 | 1.00 | 0.51 | 1.228 | 1.14 |
| 300...... | 0.466 | 2.06 | 0.99 | 0.48 | 1.310 | 1.16 |
| 400...... | 0.494 | 2.30 | 0.93 | 0.48 | 1.403 | 1.04 |
| 600...... | 0.494 | 2.56 | 0.93 | 0.45 | 1.553 | 1.07 |
| 800...... | 0.496 | 2.83 | 0.96 | 0.44 | 1.702 | 1.09 |
| 1200...... | 0.450 | 2.92 | 1.04 | 0.40 | 1.907 | 1.00 |
| 1600...... | 0.466 | 3.29 | 1.07 | 0.40 | 2.138 | 1.07 |
| 2400...... | 0.429 | 3.37 | 1.12 | 0.36 | 2.394 | 1.12 |
| 3200...... | 0.388 | 3.30 | 1.16 | 0.33 | 2.572 | 1.14 |

to integrate over all $\log \sigma^{-1}$ to account for all of the dark matter in halos. The integral of equation (3) over all $\log \sigma^{-1}$ implies an infinite mass density. In this Appendix we present an alternative fitting function that is normalized such that

$$\int g(\sigma)\, d\ln \sigma^{-1} = 1 \tag{C1}$$

for all values of $\Delta$ at $z = 0$. We focus on equation (3) for our main results because the parameters of that function vary more smoothly and monotonically with $\Delta$, and incorporating redshift evolution into that function is more straightforward and more accurate. Because we can only calibrate our mass function to $\log \sigma^{-1} \gtrsim -0.6$, the behavior of the fitting function at lower masses is arbitrary. Thus, it is not to be expected that the fitting function in this Appendix is more or less accurate than equation (3) below this calibration limit, merely that the function is better behaved.

With these caveats in mind, we find that at $z = 0$ a function of the form

$$g(\sigma) = B\left[\left(\frac{\sigma}{e}\right)^{-d} + \sigma^{-f}\right] e^{-g/\sigma^2} \tag{C2}$$

yields nearly identical results to those presented in Figure 7. Equation (C2) has four free parameters, with $B$ set by the normalization constraint from equation (C1). Expressed in terms of the parameters of equation (C2), the normalization parameter is

$$B = 2\left[e^d g^{-d/2}\Gamma\left(\frac{d}{2}\right) + g^{-f/2}\Gamma\left(\frac{f}{2}\right)\right]^{-1}. \tag{C3}$$

We follow the same procedure for fitting the model to the data as in § 2.4. Best-fit parameters are listed in Table 4. The $\chi^2/\nu$ values are similar to the values listed in Table 2.

Another requirement of the halo model is that dark matter be unbiased with respect to itself. This requires a recalibration of the large-scale halo bias function, which we investigate in another paper (J. Tinker et al., in preparation).

REFERENCES

Albrecht, A., et al. 2006, preprint (astro-ph/0609591)
Arnaud, M., Pointecouteau, E., & Pratt, G. W. 2007, A&A, 474, L37
Bialek, J. J., Evrard, A. E., & Mohr, J. J. 2001, ApJ, 555, 597
Bond, J. R., Cole, S., Efstathiou, G., & Kaiser, N. 1991, ApJ, 379, 440
Bullock, J. S., Kolatt, T. S., Sigad, Y., Somerville, R. S., Kravtsov, A. V., Klypin, A. A., Primack, J. R., & Dekel, A. 2001, MNRAS, 321, 559
Cohn, J. D., & White, M. 2008, MNRAS, 385, 2025
Cole, S., & Lacey, C. 1996, MNRAS, 281, 716
Colín, P., Klypin, A., Valenzuela, O., & Gottlöber, S. 2004, ApJ, 612, 50
Cooray, A., & Sheth, R. 2002, Phys. Rep., 372, 1
Crocce, M., Pueblas, S., & Scoccimarro, R. 2006, MNRAS, 373, 369
da Silva, A. C., Kay, S. T., Liddle, A. R., & Thomas, P. A. 2004, MNRAS, 348, 1401
Dalal, N., Doré, O., Huterer, D., & Shirokov, A. 2008, Phys. Rev. D, 77, 123514
Dolag, K., Bartelmann, M., Perrotta, F., Baccigalupi, C., Moscardini, L., Meneghetti, M., & Tormen, G. 2004, A&A, 416, 853
Evrard, A. E., et al. 2002, ApJ, 573, 7
Fakhouri, O., & Ma, C.-P. 2008, MNRAS, 386, 577
Gao, L., White, S. D. M., Jenkins, A., Stoehr, F., & Springel, V. 2004, MNRAS, 355, 819
Gottlöber, S., & Yepes, G. 2007, ApJ, 664, 117
Grossi, M., Dolag, K., Branchini, E., Matarrese, S., & Moscardini, L. 2007, MNRAS, 382, 1261
Habib, S., Heitmann, K., Higdon, D., Nakhleh, C., & Williams, B. 2007, Phys. Rev. D, 76, 083503

Haiman, Z., Mohr, J. J., & Holder, G. P. 2001, ApJ, 553, 545
Holder, G., Haiman, Z., & Mohr, J. J. 2001, ApJ, 560, L111
Hu, W., & Kravtsov, A. V. 2003, ApJ, 584, 702
Jenkins, A., Frenk, C. S., White, S. D. M., Colberg, J. M., Cole, S., Evrard, A. E., Couchman, H. M. P., & Yoshida, N. 2001, MNRAS, 321, 372
Knox, L., Song, Y.-S., & Tyson, J. A. 2006, Phys. Rev. D, 74, 023512
Koester, B. P., et al. 2007, ApJ, 660, 239
Komatsu, E., et al. 2008, ApJS, submitted (arXiv: 0803.0547)
Kravtsov, A. V., Berlind, A. A., Wechsler, R. H., Klypin, A. A., Gottlöber, S., Allgood, B., & Primack, J. R. 2004, ApJ, 609, 35
Kravtsov, A. V., Klypin, A. A., & Khokhlov, A. M. 1997, ApJS, 111, 73
Kravtsov, A. V., Vikhlinin, A., & Nagai, D. 2006, ApJ, 650, 128
Lacey, C., & Cole, S. 1994, MNRAS, 271, 676
Lee, J., & Shandarin, S. F. 1998, ApJ, 500, 14
Lima, M., & Hu, W. 2004, Phys. Rev. D, 70, 043504
———. 2005, Phys. Rev. D, 72, 043006
———. 2007, Phys. Rev. D, 76, 123013
Lin, Y.-T., Mohr, J. J., & Stanford, S. A. 2004, ApJ, 610, 745
Lukic, Z., Heitmann, K., Habib, S., Bashinsky, S., & Ricker, P. M. 2007, ApJ, 671, 1160
Majumdar, S., & Mohr, J. J. 2003, ApJ, 585, 603
———. 2004, ApJ, 613, 41
Maughan, B. J. 2007, ApJ, 668, 772
Mohr, J. J., Mathiesen, B., & Evrard, A. E. 1999, ApJ, 517, 627
Moore, B., Ghigna, S., Governato, F., Lake, G., Quinn, T., Stadel, J., & Tozzi, P. 1999, ApJ, 524, L19

Motl, P. M., Hallman, E. J., Burns, J. O., & Norman, M. L. 2005, ApJ, 623, L63

Nagai, D. 2006, ApJ, 650, 538

Navarro, J. F., Frenk, C. S., & White, S. D. M. 1997, ApJ, 490, 493

Press, W. H., & Schechter, P. 1974, ApJ, 187, 425

Press, W. H., Teukolsky, S. A., Vetterling, W. T., & Flannery, B. P. 1992, Numerical Recipes in C: The Art of Scientific Computing (2nd ed.; Cambridge: Cambridge Univ. Press)

Reed, D., Gardner, J., Quinn, T., Stadel, J., Fardal, M., Lake, G., & Governato, F. 2003, MNRAS, 346, 565

Reed, D. S., Bower, R., Frenk, C. S., Jenkins, A., & Theuns, T. 2007, MNRAS, 374, 2

Rudd, D. H., Zentner, A. R., & Kravtsov, A. V. 2008, ApJ, 672, 19

Rykoff, E. S., et al. 2008, ApJ, 675, 1106

Scoccimarro, R. 1998, MNRAS, 299, 1097

Sheldon, E. S., et al. 2007, ApJ, submitted (arXiv: 0709.1153)

Sheth, R. K., & Tormen, G. 1999, MNRAS, 308, 119

Spergel, D. N., et al. 2003, ApJS, 148, 175

———. 2007, ApJS, 170, 377

Springel, V. 2005, MNRAS, 364, 1105

Vikhlinin, A., Kravtsov, A., Forman, W., Jones, C., Markevitch, M., Murray, S. S., & Van Speybroeck, L. 2006, ApJ, 640, 691

Warren, M. S., Abazajian, K., Holz, D. E., & Teodoro, L. 2006, ApJ, 646, 881

Warren, M. S., & Salmon, J. K. 1993, in Supercomputing '93 (Los Alamitos: IEEE)

Weller, J., Battye, R. A., & Kneissl, R. 2002, Phys. Rev. Lett., 88, 231301

White, M. 2001, A&A, 367, 27

———. 2002, ApJS, 143, 241

Yepes, G., Sevilla, R., Gottlöber, S., & Silk, J. 2007, ApJ, 666, L61

Zehavi, I., et al. 2005, ApJ, 630, 1

Zentner, A. R., Rudd, D. H., & Hu, W. 2007, Phys. Rev. D, 77, 043507

Zhang, Y.-Y., Finoguenov, A., Böhringer, H., Kneib, J.-P., Smith, G. P., Kneissl, R., Okabe, N., & Dahle, H. 2008, A&A, 482, 451